

Rochester Institute of Technology

RIT Digital Institutional Repository

Theses

5-6-2015

Integrated Cardiac Electromechanics: Modeling and Personalization

Hongda Mao

Follow this and additional works at: <https://repository.rit.edu/theses>

Recommended Citation

Mao, Hongda, "Integrated Cardiac Electromechanics: Modeling and Personalization" (2015). Thesis. Rochester Institute of Technology. Accessed from

This Dissertation is brought to you for free and open access by the RIT Libraries. For more information, please contact repository@rit.edu.

Integrated Cardiac Electromechanics: Modeling and Personalization

by

Hongda Mao

A dissertation submitted in partial fulfillment of the
requirements for the degree of
Doctor of Philosophy
in Computing and Information Sciences

B. Thomas Golisano College of Computing and
Information Sciences

Rochester Institute of Technology
Rochester, New York
May 6th, 2015

©Copyright by Hongda Mao, 2015.

All rights reserved.

Integrated Cardiac Electromechanics: Modeling and Personalization

by

Hongda Mao

Abstract

Cardiac disease remains the leading cause of morbidity and mortality in the world. A variety of heart diagnosis techniques have been developed during the last century, and generally fall into two groups. The first group evaluates the electrical function of the heart using electrophysiological data such as electrocardiogram (ECG), while the second group aims to assess the mechanical function of the heart through medical imaging data. Nevertheless, the heart is an integrated electromechanical organ, where its cyclic pumping arises from the synergy of its electrical and mechanical function which requires first to be electrically excited in order to contract. At the same time, cardiac electrical function experiences feedback from mechanical contraction. This inter-dependent relationship determines that neither electrical function nor mechanical function alone can completely reflect the pathophysiological conditions of the heart.

The aim of this thesis is working towards building an integrated framework for heart diagnosis through evaluation of electrical and mechanical functions simultaneously. The basic rational is to obtain quantitative interpretation of a subject-specific heart system by combining an electromechanical heart model and individual clinical measurements of the heart. To this end, we first develop a biologically-inspired mathematical model of the heart that provides a general, macroscopic description of

cardiac electromechanics. The intrinsic electromechanical coupling arises from both excitation-induced contraction and deformation-induced mechano-electrical feedback. Then, as a first step towards a fully electromechanically integrated framework, we develop a model-based approach for investigating the effect of cardiac motion on noninvasive transmural imaging of cardiac electrophysiology. Specifically, we utilize the proposed heart model to obtain updated heart geometry through simulation, and further recover the electrical activities of the heart from body surface potential maps (BSPMs) by solving an optimization problem.

Various simulations of the heart have been performed under healthy and abnormal conditions, which demonstrate the physiological plausibility of the proposed integrated electromechanical heart model. What's more, this work presents the effect of cardiac motion to the solution of noninvasive estimation of cardiac electrophysiology and shows the importance of integrating cardiac electrical and mechanical functions for heart diagnosis. This thesis also paves the road for noninvasive evaluation of cardiac electromechanics.

Acknowledgements

First of all, I would like to thank my advisor, Dr. Pengcheng Shi, for his academic guidance, extraordinary support and endless encouragement during my doctoral study. Dr. Shi introduced me into the field of medical image computing and computational cardiology. His vision and experience have guided me throughout my research during which time he provided numerous invaluable suggestions. It was a great pleasure for me to conduct this dissertation under his supervision.

I am very grateful to Dr. Anne Haake, Dr. Linwei Wang and Dr. Shanchieh Jay Yang for their willingness to serve on my dissertation committee. Moreover, they give me lots of good suggestions to improve my thesis. In addition, special thanks go to Dr. jim Vallino being my dissertation defense chairman.

I would also like to thank all the colleagues and friends in Computational Biomedicine Laboratory of Rochester Institute of Technology: Mohamed Elshrif, Dr. Fei Gao, Dr. Zhenghui Hu, Dr. Huafeng Liu, Azar Rahimi, Dr. Linwei Wang, Dr. Ken C.L. Wong, Dr. Jijie Xu and Jingjia Xu, for their always ready to help during my six years' life in Rochester. Thanks also go to my fellow friends in both USA and China who have endured and shared the ups and downs in my Ph.D life.

Special thank goes to the Shi's: Dr.Shi, Hope, Grace and Joyce. You are my second family.

Finally, I thank my mum and sister for everything. And of course I thank my wife Min for her support, understanding and love during the past few years. You are always my source of strength.

I would like to dedicate my thesis to my family.

Contents

1	Introduction	1
1.1	The problems	4
1.1.1	Modeling of cardiac electromechanics	4
1.1.2	The effect of cardiac motion on noninvasive reconstruction of transmural cardiac electrophysiology	6
1.2	Thesis contributions	7
1.3	Thesis organization	7
2	Background	8
2.1	Cardiac anatomy	8
2.2	Cardiac physiology	11
2.3	Cardiac diagnosis	12
2.3.1	Cardiac electrical function	13
2.3.2	Cardiac mechanical function	14
2.4	Computational modeling of the heart	15
3	Modeling of cardiac electromechanics	20

3.1	Introduction	20
3.2	Modeling of cardiac electromechanics	21
3.2.1	Cardiac electrophysiology	22
3.2.2	Cardiac mechanics	28
3.2.3	Cardiac system dynamics	35
3.2.4	Heart representation	35
3.3	Experimental results	37
3.3.1	Synthetic data	37
3.3.2	Physiological simulation	40
3.3.3	Pathological simulation	43
4	The effect of cardiac motion on noninvasive transmural imaging of cardiac electrophysiology	52
4.1	Introduction	52
4.2	Forward problem	54
4.2.1	Coupled heart-torso representation	54
4.2.2	TMPs-to-BSPMs mapping	55
4.3	Inverse problem	57
4.4	Experimental results	58
4.4.1	The effect of cardiac motion on the forward problem	58
4.4.2	The effect of cardiac motion on the inverse problem	63
4.5	Discussion and conclusion	68
5	Understanding of embryonic heart morphogenesis based on robust	

image segmentation	71
5.1 Introduction	71
5.2 Methodology	74
5.2.1 Image acquisition	74
5.2.2 Image formation	76
5.2.3 Image Segmentation	77
5.3 Experimental results	82
5.3.1 Data	82
5.3.2 Evaluation of automatic segmentation	82
5.3.3 EHM study	84
5.4 Conclusion	85
6 Summary and future work	87
6.1 Modeling of cardiac electromechanics	88
6.2 The effect of cardiac motion on noninvasive transmural imaging of cardiac electrophysiology	89
6.3 Embryonic heart morphogenesis	90

List of Tables

5.1	DSC values that measure the overlap between the two manual segmentation, the first manual segmentation against automatic segmentation, and the second manual segmentation against automatic segmentation	82
5.2	Average volume of the whole heart and the luminal space at different stages of development. (mm^3)	85

List of Figures

2.1	Historical outline of human heart with vessels and lungs within the chest. Image from http://pantip.com/topic/30566994	9
2.2	Macroscopic structure of the heart. Image from http://www.surry.edu/Portals/	10
2.3	Cardiac events occurring in the cardiac cycle. Two complete cycles are illustrated. Image from http://www.healthanalytics.us/2013/11/04	12
2.4	Schematic diagram of normal sinus rhythm for a human heart as seen on ECG. Image from http://a-fib.com/	14
2.5	Clinical 12-lead ECG signals. Image from http://hqmeded-ecg.blogspot.com/	15
2.6	Atrial fibrillation. Image from http://lifeinthefastlane.com/ecg-library/atrial-fibrillation/	16
2.7	(a) - (f) cardiac MR images acquired at same time while different positions along the short axis of the heart	18

2.8	Cardiac MR images acquired at same position while different time frames	19
3.1	The motion of a point x from time t_0 to time t_s	22
3.2	Heterogeneity of TMP shapes in endocardium, myocardium and epicardium	26
3.3	Time-vary active stress	29
3.4	Meshfree particle representation of the computational domain of the heart	36
3.5	Simulation of the proposed heart model on a cubic object. From top row to bottom: electromechanics, strain maps along fiber, strain maps along fiber cross and strain maps along fiber cross. From Left to right with time: 0ms, 13ms, 110ms, 140ms, and 148ms (white lines indicate fiber orientations, the colors represent normalized TMP and strain values.)	38
3.6	The 17 segments and the nomenclature of the left-ventricular myocardium recommended by the American Heart Association, shown on a circumferential polar plot [37]	45
3.7	Simulation of cardiac electromechanics. the color indicates normalized TMP. From left to right and top to bottom. The time for the snapshots are at 0ms, 5ms, 10ms, 20ms, 40ms, 55ms, 75ms, 95ms, 110ms, 125ms, 130ms, 135ms, 140ms, 145ms, 195ms, 430ms	46

3.8	Radial strain maps. The time for the snapshots are at 0ms, 5ms, 10ms, 20ms, 40ms, 55ms, 75ms, 95ms, 110ms, 125ms, 130ms, 135ms, 140ms, 145ms, 195ms, 430ms	47
3.9	Circumferential strain maps. The time for the snapshots are at 0ms, 5ms, 10ms, 20ms, 40ms, 55ms, 75ms, 95ms, 110ms, 125ms, 130ms, 135ms, 140ms, 145ms, 195ms, 430ms	48
3.10	Comparison between simulation results of left ventricle volume change curve and single-lead ECG	49
3.11	Simulation of LBBB	50
3.12	Cardiac cycle simulation under LBBB condition. The time for the snapshots are at 0ms, 5ms, 10ms, 20ms, 40ms, 55ms, 75ms, 95ms, 110ms, 125ms, 130ms, 135ms, 140ms, 145ms, 195ms, 430ms	50
3.13	Simulation under myocardium infarction. The time for the snapshots are at 0ms, 5ms, 10ms, 20ms, 40ms, 55ms, 75ms, 95ms, 110ms, 125ms, 130ms, 135ms, 140ms, 145ms, 195ms, 430ms	51
3.14	Cardiac cycle simulation under myocardium infarction condition . . .	51
4.1	Meshfree-BEM representation of the heart-torso structure	56
4.2	Simulation results comparison between static heart model and our electromechanical model. left to right with time, 1 ms, 18 ms, 72 ms, 255 ms, and 288ms. The color indicates normalized TMP values . . .	60
4.3	Normal 12-lead ECG simulation, blue: static heart model; red: our proposed heart model	62
4.4	left: TMP; right: BSPMs	63

4.5	TMP reconstruction on a normal heart. From left to right, the first three columns are at depolarization phase, the last two columns are at repolarization phase	64
4.6	TMP reconstruction at different time. Left: 10ms after the onset of ventricular depolarization; Right: 130ms after the onset of ventricular depolarization. The colors are manually tuned to have a good visual comparison, they only reflect the pattern of the TMP distribution but not the true value	65
4.7	Statistical analysis of noninvasive transmural imaging accuracy on healthy heart based on correlation coefficient	66
4.8	The heart with post-myocardium infarction. Blue: infarcted region; red: normal region	67
4.9	TMP reconstruction at different time. Left: 10ms after the onset of ventricular depolarization; Right: 130ms after the onset of ventricular depolarization. The colors are manually tuned to have a good visual comparison, they only reflect the pattern of the TMP distribution but not the true value	69
4.10	Statistical analysis of noninvasive transmural imaging accuracy on the heart with myocardium infarction based on correlation coefficient	70
5.1	3D view of embryonic quail hearts. From left to right: day 6, day 8 and day 14	74

- 5.2 Visual comparison between manual segmentation and automatic segmentation.
- (a) original 3D image and three slices in different views. (b) manual segmentation done by the first biologist. (c) manual segmentation done by the second biologist. (d) automatic segmentation. 86
- 5.3 3D segmentation of one group of the hearts. Columns from left to right are the heart at day 6, 7, 8, 9 and 14. For visualization purpose, the outer boundary is rendered as transparent. (L: left ventricle. R: right ventricle) 86

Chapter 1

Introduction

Cardiac disease, with its complications, remains the leading cause of morbidity and mortality in the world, contributing significantly to the global healthcare expenditure [1]. For example, a snapshot of the population would reveal that half a million people yearly die because of various cardiac diseases in the United States, such as cardiac arrhythmias [2]. Although a large body of research has been devoted to gaining insight into the mechanisms behind the healthy and aberrant behaviors of the heart [3, 4, 5, 6, 7, 8], significant gaps in knowledge are still present due to the complexity of heart structure and the sophisticated electromechanically integrated behaviors of the heart.

In the clinical setting, a variety of heart diagnosis techniques have been developed during the last century, which fall into two groups. One group typically evaluates the electrical function of the heart. For example, a patient is commonly evaluated either noninvasively by electrical potentials on the body surface, such as an electrocardio-

gram (ECG) [9], or invasively by catheter-based mapping techniques [10]. All these approaches used for heart diagnosis typically ignore cardiac mechanical function. On the other hand, another group assesses the mechanical function of the heart. Cardiac mechanical function is assessed by measuring the volume of heart chambers, blood pressure or ejection fraction through advanced medical imaging techniques, such as magnetic resonance imaging (MRI) [11], computed tomography (CT) [12], and ultrasound imaging [13]. Because the acquisition of 3D medical images occurs at a larger temporal scale compared to electrical signal collection, the information of cardiac electrical activity occurs between two image frames is lost. As a result, to the best of our knowledge, there does not exist any clinical heart diagnosis technique that can evaluate electrical and mechanical functions simultaneously.

Nevertheless, the heart is an electromechanical organ, its cyclic pumping arises from the synergy of its electrical and mechanical function, which requires first to be electrically activated in order to contract. At the same time, cardiac electrical function experiences the feedback from cardiac mechanical contraction [14, 15]. This inter-dependent relationship determines that neither electrical function nor mechanical function alone can completely reflect the pathophysiological behaviors of the heart. For example, for two thirds of patients, heart attack cannot be detected by ECG[16], and patients with long or short QT syndrome presents normal mechanical activity so would not be diagnosed if only mechanical activity were measured [17]. Cardiac electromechanics, the integrated electrical and mechanical function of the heart, becomes of great clinical interest because it allows concurrent electromechanical imaging and could advance current clinical practice where the

electrical and mechanical function is evaluated separately. However, cardiac electrical and mechanical signals belong to two different modalities, and therefore, it is not straightforward to obtain cardiac electromechanics by simply combining electrical and mechanical measurements through conventional data fusion techniques [18]. What's more, current clinical measurements, either used for evaluating electrical or mechanical functions, are typically sparse and corrupted with noises from various sources [19, 20]. A novel way to measure cardiac electromechanics is badly needed.

Thanks to the development of computational power and mathematical modeling, computational modeling of the heart has been a powerful tool for understanding the mechanisms behind cardiac electrical and mechanical activities [21, 22, 23]. Computational models allow, on one hand, reproducing some biological phenomena through in-silico simulation, such as cardiac electrical wavefront propagation. On the other hand, these models can serve as testing environments for predictive analysis of heart activities that can help in understanding the complex relationship between causes and effects. More importantly, computational models can serve as a central link for connecting to clinical measurements of different modalities [18, 24, 20].

In view of this, the primary objectives of this research are to (1) develop a biologically-inspired mathematical model for cardiac electromechanics simulation, and (2) use this model to understand the effect of cardiac motion on noninvasive reconstruction of transmural cardiac electrophysiology.

1.1 The problems

1.1.1 Modeling of cardiac electromechanics

Modeling and simulation have long been intertwined with cardiac research. Appropriate models and simulation can help interpret an array of experimental data and dissect important mechanisms and interrelationships. Due to the electromechanically integrated property of the heart, a complete mathematical heart model should contain two interconnected components: cardiac electrophysiology and cardiac mechanics [25]. Cardiac electrophysiology details the spatiotemporal dynamics of electrical wave propagation within the heart domain as well as the effect of mechano-electrical feedback. Cardiac mechanics describes attributes of the myocardium and the deformation related to the active contraction stresses caused by electrical activation.

However, most of the existing models do not contain both components. On one hand, a variety of models composed of a cardiac electrophysiological model have been widely used in personalized cardiac electrophysiology (EP) simulation and recovery [26, 27]. The major drawback of these models is the mechanical function of the heart is ignored because of the assumption the the heart is static during the cardiac cycle. On the other hand, a type of so-called "one-way" electromechanical coupling model was popularly used in heart activity modeling [22, 28] and model-guided cardiac motion tracking [22, 11]. In these works, electrical activity was first determined by the solution of a cardiac electrophysiological model and then was treated as an input for mechanical activity. Although the effect of electromechani-

cal coupling is considered, the effect of mechanoelectrical feedback was ignored. In [29], the authors proposed an integrated heart model that included both electrical and mechanical components. Based on the results of simulations, the authors found that heart motion contributed significantly to the spatiotemporal dynamics of electrical wave propagation. However, the assumption of isotropic and homogeneous myocardium material properties limited its application in practice. Moreover, the simulations were only conducted on two-dimensional synthetic data without testing on any realistic three-dimensional heart geometry. More recently, some more complex models coupled a cellular electrophysiology model and an active mechanics model for cardiac electromechanics simulation were proposed [30, 31]. However, it is not practical to measure ion concentrations in clinical environment, which limits these models to the research laboratory. What's more, these model typically have a great number of parameters which makes it is infeasible to tackle inverse problem which we are interested.

In view of the problems, we develop an electromechanical model for simulation of cardiac electromechanics. The model includes both inter-connected components which can provide a general, macroscopic description of the heart activity. To keep a balance of computational feasibility and physiological plausibility, we have adopted phenomenological models for each component.

1.1.2 The effect of cardiac motion on noninvasive reconstruction of transmural cardiac electrophysiology

Body surface potential (BSP) recordings, such as ECG, noninvasively reflects the underlying cardiac electrical activity has been a standard tool for heart diagnosis in clinic since last century. Nevertheless, the measurement is typically limited in spatial resolution and only remotely reflects the electrical activity of the heart, which limits its functionality for heart diagnosis. For example, for two thirds of patients, heart attack cannot be detected by ECG [16]. To overcome this drawback, noninvasive reconstruction of transmural cardiac electrophysiology by combining a cardiac electrophysiological model and body surface potential maps (BSPMs) has attracted a lot of attention over the last decade [7, 26, 24]. In these works, detailed 3D cardiac electrical activity is reconstructed by given BSPMs and heart geometry from medical images. The results of these works are very encouraging because they can not only provide transmural electrical propagation information but provide the location and size of abnormal regions as well. Nevertheless, all the existing works are based on the assumption that the heart is static during the cardiac cycle. In other words, the effect of cardiac motion on electrical function has been ignored.

Some works have been proposed to investigate the effect of cardiac motion on the inverse problem of cardiac electrophysiology [32, 33, 34]. However, all of them focused on the electrical activity on the epicardium instead of the transmural information. In this thesis, we will investigate the effect of cardiac motion on noninvasive reconstruction of transmural cardiac electrophysiology by combining our proposed

electromechanical heart model and BSPMs.

1.2 Thesis contributions

There are three major contributions in this thesis:

- Developed a mathematical model for simulation of cardiac electromechanics.
- Developed a regularization constraint approach for investigating the effect of cardiac motion on noninvasive reconstruction of transmural cardiac electrophysiology by combining the proposed heart model and BSPMs.
- Developed a convex optimization approach based image segmentation method for understanding embryonic heart morphogenesis from confocal microscopy imaging.

1.3 Thesis organization

The thesis is organized as follows: Chapter 2 reviews the background of cardiac anatomy, physiology and modeling. Chapter 3 presents the development and experimental validations of modeling of cardiac electromechanics. Based on the electromechanical model, we investigate the effect of cardiac motion to noninvasive reconstruction of transmural cardiac electrophysiology in Chapter 4. Chapter 5 presents the work of understanding of embryonic heart morphogenesis based on confocal microscopy imaging and robust image segmentation. The thesis ends with conclusion and future work in chapter 6.

Chapter 2

Background

In this chapter, we will review the background of heart anatomy, physiology and diagnosis. Moreover, we also give an introduction of the state-of-the-art works on computational modeling of the heart.

2.1 Cardiac anatomy

The heart is one of the most important organs in the human body, it has a mass of between 250 and 350 grams and is about the size of a fist. It is located in the chest between the two lungs and surrounded by a layer called the pericardium, which is composed of fat and tissue as shown in Fig. 2.1. When a person is in the supine position, the heart is a conical structure that lies relatively horizontally with the atria at its base and the ventricles at its apex. During the cardiac cycle, the heart rotates over its long axis, the right atrium and ventricle are more anterior than the left chambers, and the right and left sides of the heart are not aligned with the

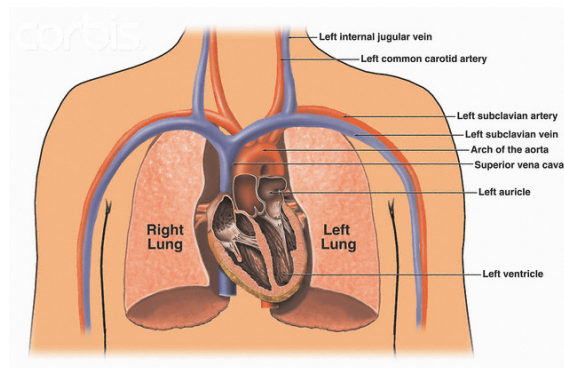


Figure 2.1: Historical outline of human heart with vessels and lungs within the chest. Image from <http://pantip.com/topic/30566994>

homonymous sides of the body [16]. The interventricular septum is almost parallel with the frontal plane, and the left ventricular free wall includes nearly 300 degrees of the left ventricular circumference and faces superiorly, posteriorly, and inferiorly.

The heart constitutes together with the blood vessels the cardiovascular system, which has the task of transporting blood in the body through cyclically pump and contraction. The anatomy is closely coupled with its physiology. Depending on the stage of development, the species, the gender and pathologies differences can be found in the anatomy [16].

From a macroscopic structural view, the heart is separated into two functionally and anatomically similar structures, left and right halves, which represents the division of the blood circulation system in two different parts [35]. A detailed human heart anatomy with four chambers, related vessels, and valves are presented in figure 2.2. The right part collects deoxygenated blood from the whole body and send it to the lungs through pulmonary artery. The left part receives oxygenated blood from the lungs and pumps it to the whole body through aorta. The left

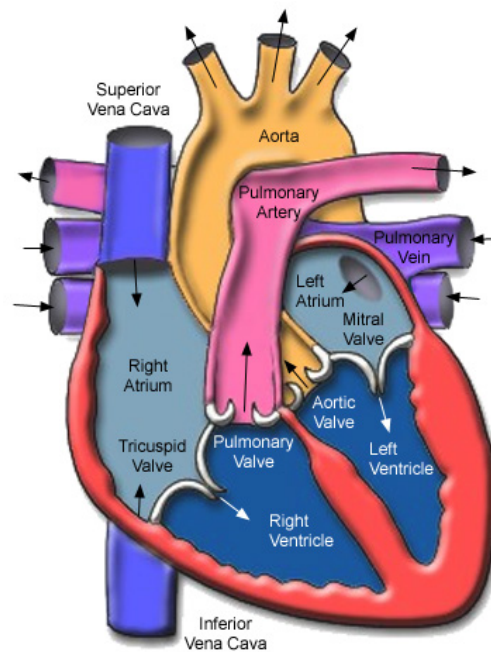


Figure 2.2: Macroscopic structure of the heart. Image from <http://www.surry.edu/Portals/>

part is larger than the right part for higher pressure in blood transportation. The halves can be further divided into upper and lower chambers: atrium and ventricle. The atria and ventricles are composed of a cavity filled by blood and a surrounded three-layer structure wall. The outside layer of the wall is termed epicardium, and the inner layer is referred to endocardium. The middle layer is a muscle structured called myocardium. The blood goes from the atria to the ventricle. To prevent the back flow of the blood from ventricle to atria, the mitral valve exists between left atrium and left ventricle, and the tricuspid valve exists between right atrium and right ventricle.

2.2 Cardiac physiology

The heart is an electromechanical organ which exhibits multi-physics behaviors which requires first to be electrically excited in order to contract. Besides its multi-physics property, it also exhibits multi-scale behaviors. In cellular level, a cardiac myocyte, heart cell, is initially excited by a large inward current of sodium, which triggers the upstroke of the action potential. Next, calcium enters the cell through L-type calcium channels and initiates release of calcium from intracellular stores, which forms intracellular calcium concentration. Followed by binding of calcium to troponin C and cross-bridge cycling [25]. The latter forms the basis for contractile protein shortening and the generation of active tension in the myocyte, which is called electromechanical coupling. Besides, intracellular calcium can also triggers calcium-activated potassium channels and forms stretch-activated currents, which is called the effect of mechanoelectrical feedback. Hence, calcium plays a key role in the interaction between cardiac electrophysiology and mechanics.

In tissue level, a normal heart cycle starts from the depolarization of the sinoatrial (SA) node located in the right atrium. The depolarization wave propagates through the atria and reaches to the atrio-ventricular (AV) node, which located near the septum between the atria and the ventricles. Distal to the AV node, the depolarization wave travels fast through His bundle and reaches Purkinje fibers. Leaving the Purkinje fibers, the depolarization wave enters to the ventricular myocardium. The myocytes are excited following the sequence of the depolarization wave, and the heart contracts accordingly.

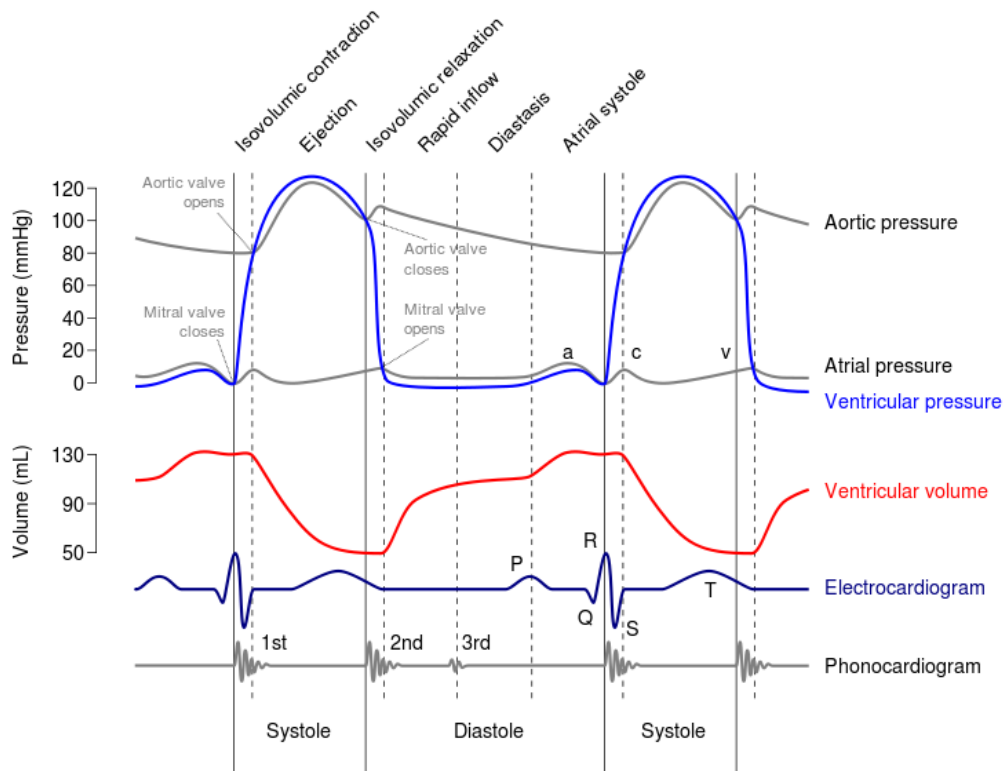


Figure 2.3: Cardiac events occurring in the cardiac cycle. Two complete cycles are illustrated. Image from <http://www.healthanalytics.us/2013/11/04>

2.3 Cardiac diagnosis

Although the heart is an electromechanical organ, in clinical setting, cardiac electrical and mechanical functions are typically evaluated separately. Mostly because cardiac electrical and mechanical signals belong to two different modalities, it is not straightforward to have fused signal which has both electrical and mechanical information. To the best of our knowledge, there does not exist any clinical diagnosis technique can measure cardiac electrical and mechanical activities simultaneously.

Figure 2.3 shows typically coordinated electrical and mechanical signals measured in clinic. In the following sections, we will introduce these measurements in details.

2.3.1 Cardiac electrical function

Cardiac electrical function is typically evaluated by the recordings of the potential maps on the body surface, such as ECG. ECG recordings remotely reflect the spatiotemporal dynamics of electrical activity within the heart [20]. A typical ECG signal for one heart beat has a shape like figure 2.4. It usually includes P-wave, QRS complex and T-wave, each of them represents different phases of a cardiac cycle. P-wave corresponds to the depolarization of the atria, during which the heart cells in the atria are excited by the electrical wave propagation from SA node to AV node. QRS complex represents the phase of the depolarization of the ventricles, during which the electrical signal leaves the AV node and quickly spreads through the ventricles throughs the purkinje fibers. T-wave corresponds to the repolarization of the ventricles.

ECG has been a standard tool for assessing the heart function in clinic. Although the number of leads for ECG recording could be different, 12-lead ECG is the most widely used. Figure 2.5 depicts a normal 12-lead ECG, where each lead exhibits regular P-QRS-T waves. We also present an abnormal ECG case with atrial fibrillation in figure 2.6. In the ECG signal with atrial fibrillation, an absent of P-wave can be observed.

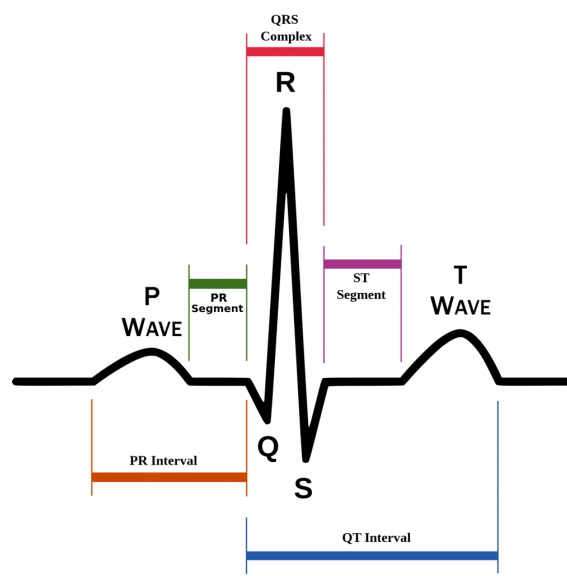


Figure 2.4: schematic diagram of normal sinus rhythm for a human heart as seen on ECG. Image from <http://a-fib.com/>

2.3.2 Cardiac mechanical function

In clinical, cardiac mechanical function is typically assessed by medical imaging such as CT, MRI and ultrasound. In figure 2.7, we present several slices of images from a 3D MR image. These images were scanned at the same time but different location. From (a) to (f), the images present the base to the apex of the ventricles. One important metric for determining normal and abnormal heart is the ejection fraction, which means the volumetric fraction of blood pumped out of the left and right ventricle with each heartbeat or cardiac cycle. To obtain this value, we need to have a volume curve as presented in figure 2.3. Thus, multiple frames of images are usually scanned during one cardiac cycle. Figure 2.8 presents several frames of images which were scanned at the approximately same location at different time. With advanced

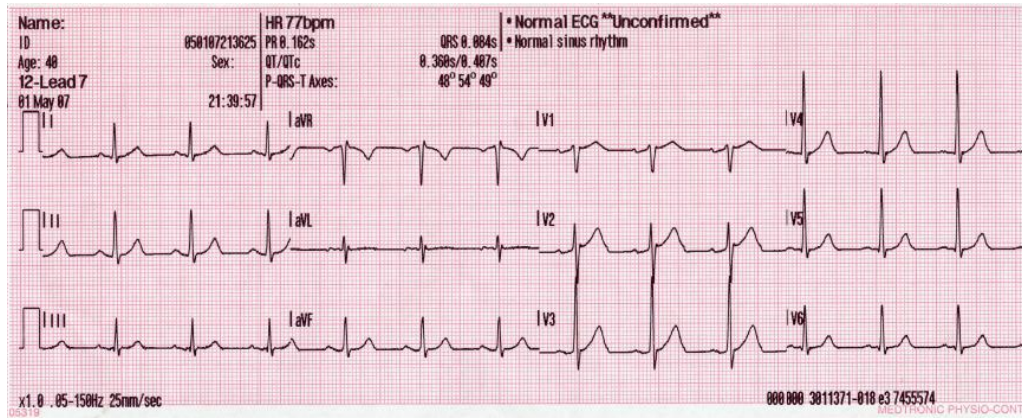


Figure 2.5: Clinical 12-lead ECG signals. Image from <http://hqmeded-ecg.blogspot.com/>

image segmentation and registration approach [36, 37, 13], the ejection fraction can be estimated, and therefore, help the doctors to make a clinical decision.

2.4 Computational modeling of the heart

Modern cardiac research has recognized that computational modeling can help interpret experimental findings and dissect important mechanisms of the heart behaviors. The heart is a highly integrated organ exhibits multi-scale (from cellular to organ level) and multi-physics (cardiac electrophysiology, cardiac mechanics and their interaction) behaviors. Because of this complexity of the heart system, most of the previous works use reductionist modeling approach that is to model either cardiac electrophysiology or cardiac mechanics by ignoring the interaction with the other [38, 25, 30].

The earliest work for modeling electrophysiology of cells is proposed by Hodgkin

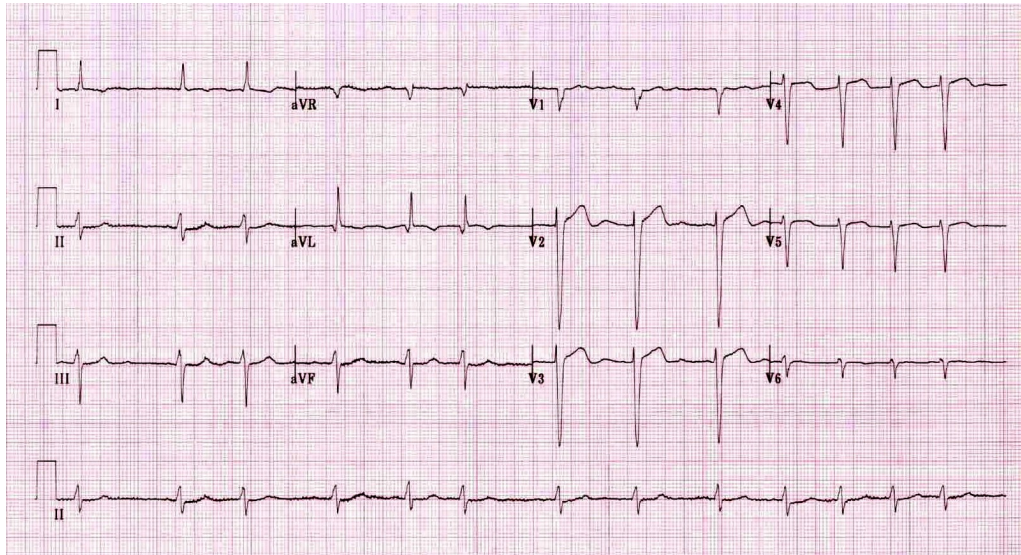


Figure 2.6: Atrial fibrillation. Image from <http://lifeinthefastlane.com/ecg-library/atrial-fibrillation/>

and Huxley half a century ago [39]. A lot of models are proposed later on to extend the seminal work [40, 41, 3], to mention a few. To model the spatiotemporal dynamics of the electrical wave propagation in cardiac tissue, these models are extended to the reaction-diffusion formulation [42, 43, 44]. A common drawback of these models is they are all based on the assumption that the heart is static during cardiac cycle by ignoring the effect of mechanoelectrical feedback. A hybrid method for studying the effect of heart motion on cardiac electrophysiology is proposed in [32], which shows that the morphologies of T-wave are quite different between heart model with and without considering heart motion.

Apart from the approaches to model pure cardiac electrophysiology, there is a class of so-called "one-way" electromechanical coupling models are widely used in cardiac electromechanical modeling [22, 28] and motion tracking [22, 11]. In these

models, electrical activity is first determined by the solution of a cardiac electrophysiological model and then be treated as an input for mechanical activity. Although the effect of electromechanical coupling is considered, the effect of mechano-electrical feedback is ignored.

There also exist some attempts to use integrated system approach to model cardiac electromechanics. Since the electromechanical coupling happens at the cellular level through calcium ions exchange, the most common approach for modeling electromechanics is by coupling a cellular electrophysiological model and a tissue level cardiac mechanical model [31, 45]. Although these models are able to describe very detail heart behaviors, they are usually computational expensive. What's more, there is no direct relationship between these models to clinical measurements, which makes them hard to be used in clinical environment. In [29], the authors propose an integrated heart model that includes both electromechanical coupling and mechano-electrical feedback. They find that the heart deformation has a significant effect on the dynamics of electrical wave propagation. However, the assumption of isotropic and homogeneous myocardium material properties limits its application. What's more, the simulations are performed only on synthetic data in two dimensional space.

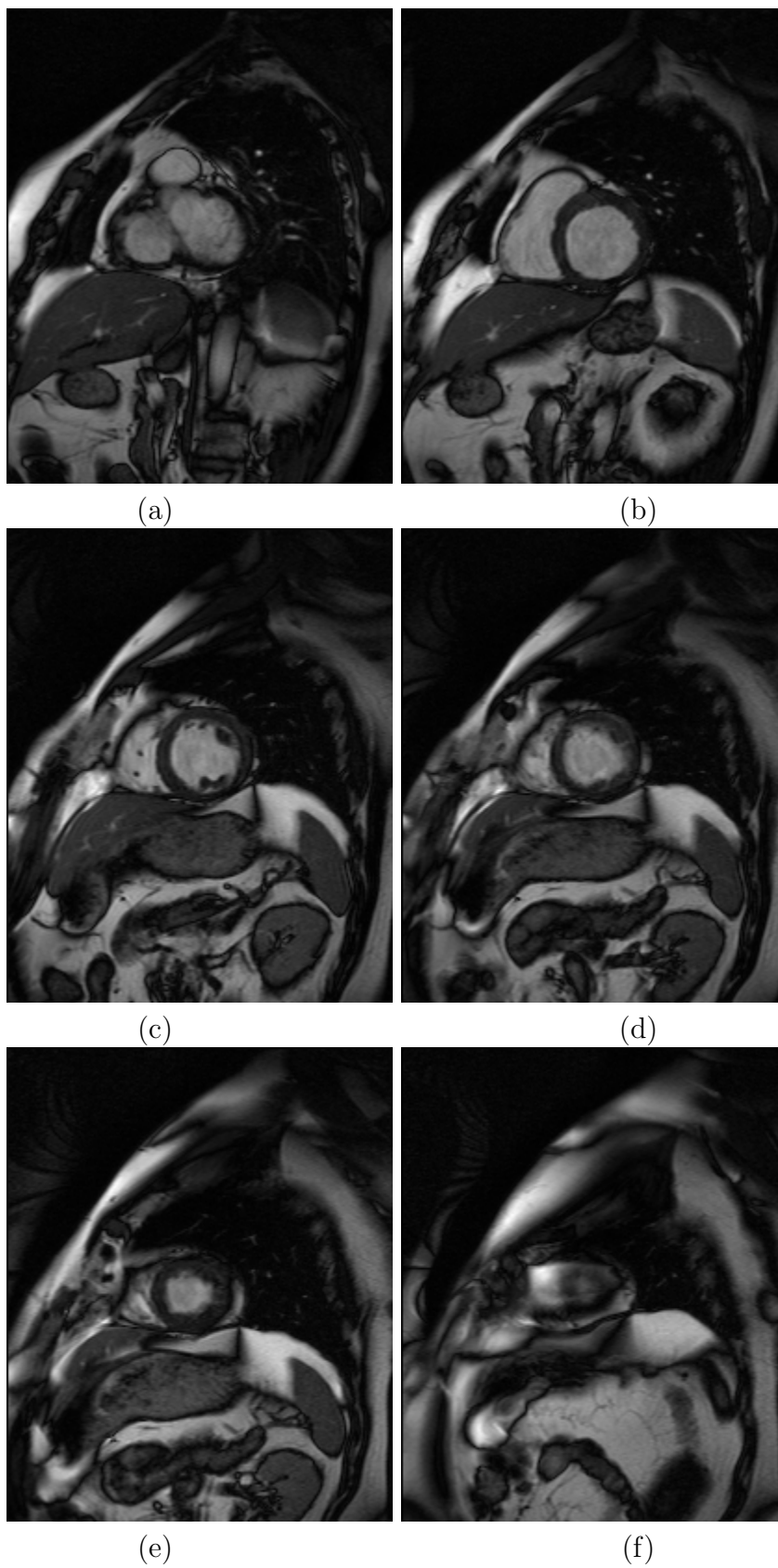


Figure 2.7: (a) - (f) cardiac MR images acquired at same time while different positions along the short axis of the heart

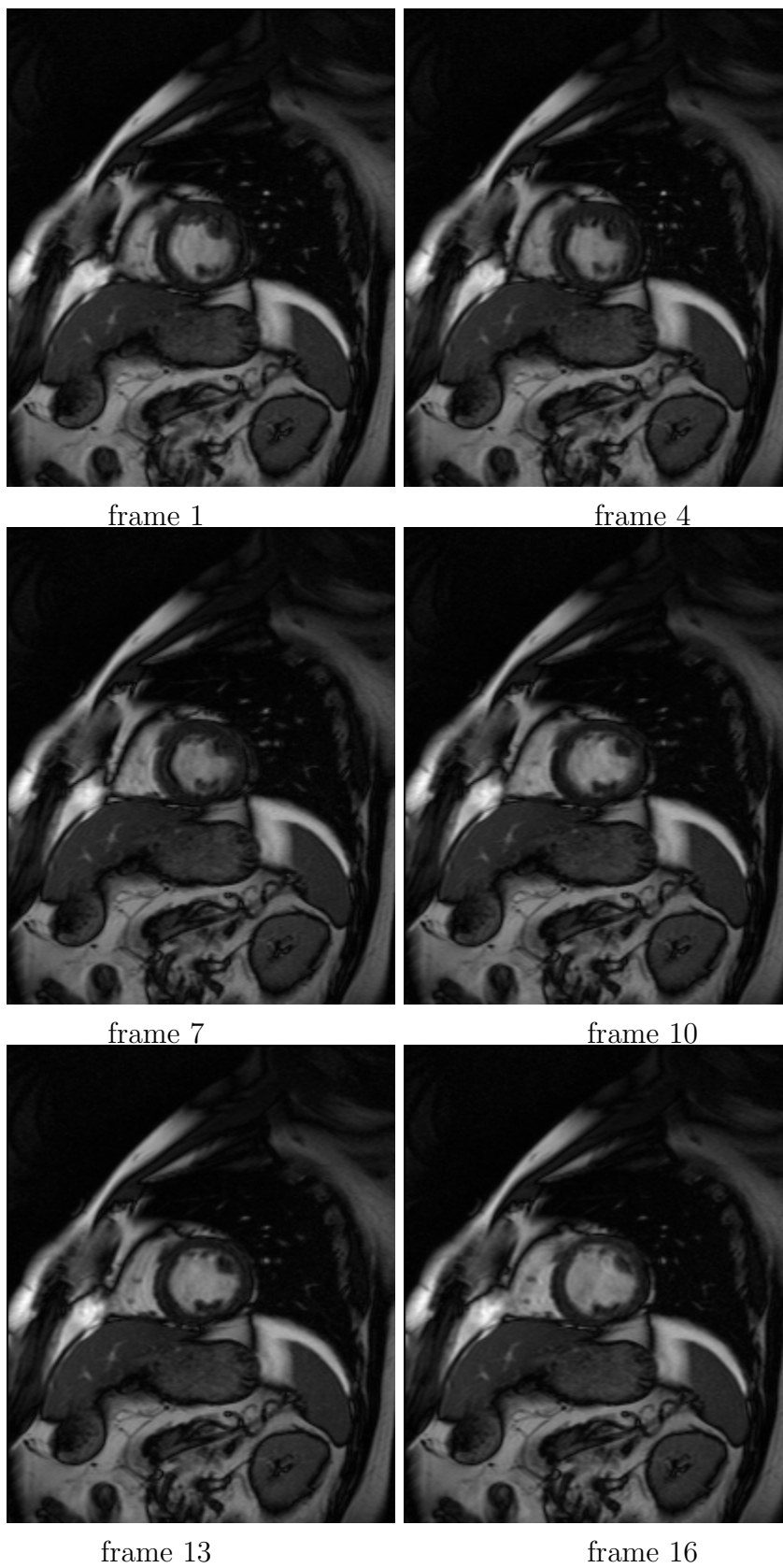


Figure 2.8: Cardiac MR images acquired at same position while different time frames

Chapter 3

Modeling of cardiac electromechanics

3.1 Introduction

Understanding of the mechanisms behind cardiac electrical and mechanical functions and their interaction has attracted great of interest in basic science and clinical cardiology [26, 31]. Experimental studies have provided significant insight into the electrical and mechanical activity of the heart from molecular up to the whole body level; nevertheless, detailed information regarding the intricate processes at each level can not capture the emergent phenomena, for example, the interaction process between electrical and mechanical activities. Moreover, the existing clinical techniques are limited by their inability to assess the 3D electrical and mechanical activity in the heart simultaneously and with sufficient spatiotemporal resolution

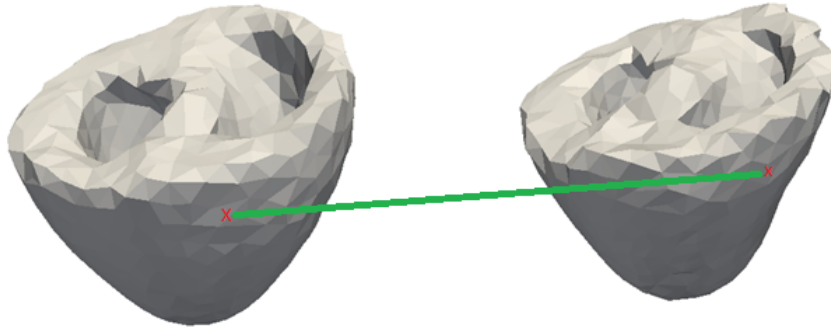
[31]. Thus a comprehensive approach that can integrate detailed information of both electrophysiology and mechanics is needed to provide a better understanding of the complex relationship between electrical and mechanical activity. Thanks to the development of computational power and mathematical modeling techniques, computational modeling of the heart represents such an approach [29, 30, 31, 25].

Due to the electromechanically integrated property of the heart, a complete mathematical heart model should contain two interconnected components: cardiac electrophysiology and cardiac mechanics [25]. Cardiac electrophysiology details the spatiotemporal dynamics of electrical wave propagation within the heart domain as well as the effect of mechano-electrical feedback which . cardiac mechanics describes attributions of the myocardium and the deformation related to the active contraction stresses which is caused by electrical activation.

To keep a balance of computational feasibility and physiological meaningfulness, we develop an electromechanical model which will be introduced in the following sections.

3.2 Modeling of cardiac electromechanics

To build a mathematical model of the heart, each point within the computational domain can be characterized by two primary field variables, nodal transmembrane potential (TMP) $v(x, t)$ and nodal displacement $u(x, t)$. where x represents the location of a point of interest and t stands for the time, as shown in figure 3.1. TMP refers to the potential difference between intracellular domain and extracellular do-



Reference geometry at time t_0 Deformed geometry at time t_s

Figure 3.1: The motion of a point x from time t_0 to time t_s

main within the context of mono-domain formulations of the cardiac electrophysiology [30, 42, 43]. The evolution of the two field variables in a spatiotemporal manner is governed by two differential equations describing cardiac electrophysiology and cardiac mechanics, respectively.

3.2.1 Cardiac electrophysiology

The spread of electrical wavefront in the heart occurs due to the excitability of individual heart cells and the propagation of electrical excitation from one cell to neighboring cells by intercellular transport of ions via gap junctions [35]. Thus, a general model for each heart cell can be represented as the following equation [46]

$$I = C_m \frac{dV}{dt} + I_{ion} + I_{SAC} \quad (3.1)$$

where I represents total transmembrane current, C_m stands for membrane capacitance per unit area, V represents TMP, I_{ion} is the total ionic transmembrane currents, and I_{SAC} stands for stretch-activated current related to the effect of mechano-electrical feedback [15].

To describe the propagation of cardiac electrical wave in myocardium, the total transmembrane current can be replaced by a reaction-diffusion term. Inherited from equation 3.1, a reaction-diffusion model can be represented as follows

$$I = \nabla \cdot (\mathbf{D}_0 \nabla V) = \frac{dV}{dt} + I_{ion} + I_{SAC} \quad (3.2)$$

Here $C_m = 1$ has been adopted as in most of the literature [29], ∇ stands for the spatial derivatives, and \mathbf{D}_0 is the diffusion tensor where d_f and d_{cf} are diffusion parameters along the fiber and cross fiber directions, which reflects different propagation speed along and cross fiber directions.

$$\mathbf{D}_0 = \begin{bmatrix} d_f & 0 & 0 \\ 0 & d_{cf} & 0 \\ 0 & 0 & d_{cf} \end{bmatrix}$$

To determine the formulation of equation 3.2, we need to know the explicit expressions of I_{ion} and I_{SAC} . I_{SAC} is the effect of mechano-electrical feedback, which will be discussed later. Based on the expression of the ionic current I_{ion} , the existing models can be roughly classified into two classes : biophysical models and phenomenological models.

Biophysical models

Biophysical models are based on direct experimental findings and detailed modeling the currents caused by different ions at the cellular level[41]. Such models generally can accurately reproduce various properties of active action potential, such as shape, action potential duration, and ionic currents. Nevertheless, it is impossible to get the measurements of ion concentrations of a specific patient in clinical environment, which limits their application in real world. Besides, models of this type typically has lots of variables and partial differential equations to solve, and therefore, needs a lot of computational resources.

Phenomenological models

Phenomenological models provide a macroscopic description of cardiac electrical wave propagation in the myocardium, which does not explicitly compute the concentrations of ions, such as Calcium, and therefore, has fewer variables and equations than biophysical models. They can usually be formulated in either a bidomain model or monodomain model [42, 43].

To simplify our problem, we will ignore stretch-activated currents I_{SAC} for now and integrate it later. In this thesis, we have selected the monodomain two-variable Aliev-Panfilov model [42] to keep a balance of computational feasibility and physiological plausibility. This model has been widely used in cardiac electrophysiology (EP) simulation [22] and cardiac EP imaging [26].

$$\begin{cases} \frac{\partial V}{\partial t} = \nabla \cdot (\mathbf{D}_0 \nabla V) + sV(V - a)(1 - V) - VC \\ \frac{\partial C}{\partial t} = -e(C + sV(V - a - 1)) \end{cases} \quad (3.3)$$

where V is a vector stands for normalized TMP, and C is a vector represents a recovery current which controls the local depolarization behavior of the action potential. Parameters a , e , and s are constants in time but not necessarily in space to determine the shape of TMP. Except for the excitability a , other parameters do not have physical meaning. In figure 3.2, we present heterogeneity of TMPs shapes in different values of excitability a which equals to 0.14, 0.15, and 0.17 at myocardium, endocardium and epicardium, respectively.

Mechanoelectrical feedback

So far, we have not considered the effect of mechanoelectrical feedback as the term I_{SAC} in equation 3.2. In practice, cardiac electrophysiology and cardiac mechanics are depended on each other, and realistic cardiac simulation can only be achieved when this inter-dependent relationship is considered [31]. Earlier experimental and clinical research has demonstrated that mechanical activity of the heart affects cardiac electrophysiology. Generally speaking, mechanical activity affects cardiac electrophysiology mainly in three ways. First, due to the heart motion, the positions of cardiac electrical sources are changing consistently during the cardiac cycle. Second, the fiber orientation of a heart cell is changing due to the heart contraction, and which directly leads to the change of conductivity tensor \mathbf{D}_0 . At last, stretch-

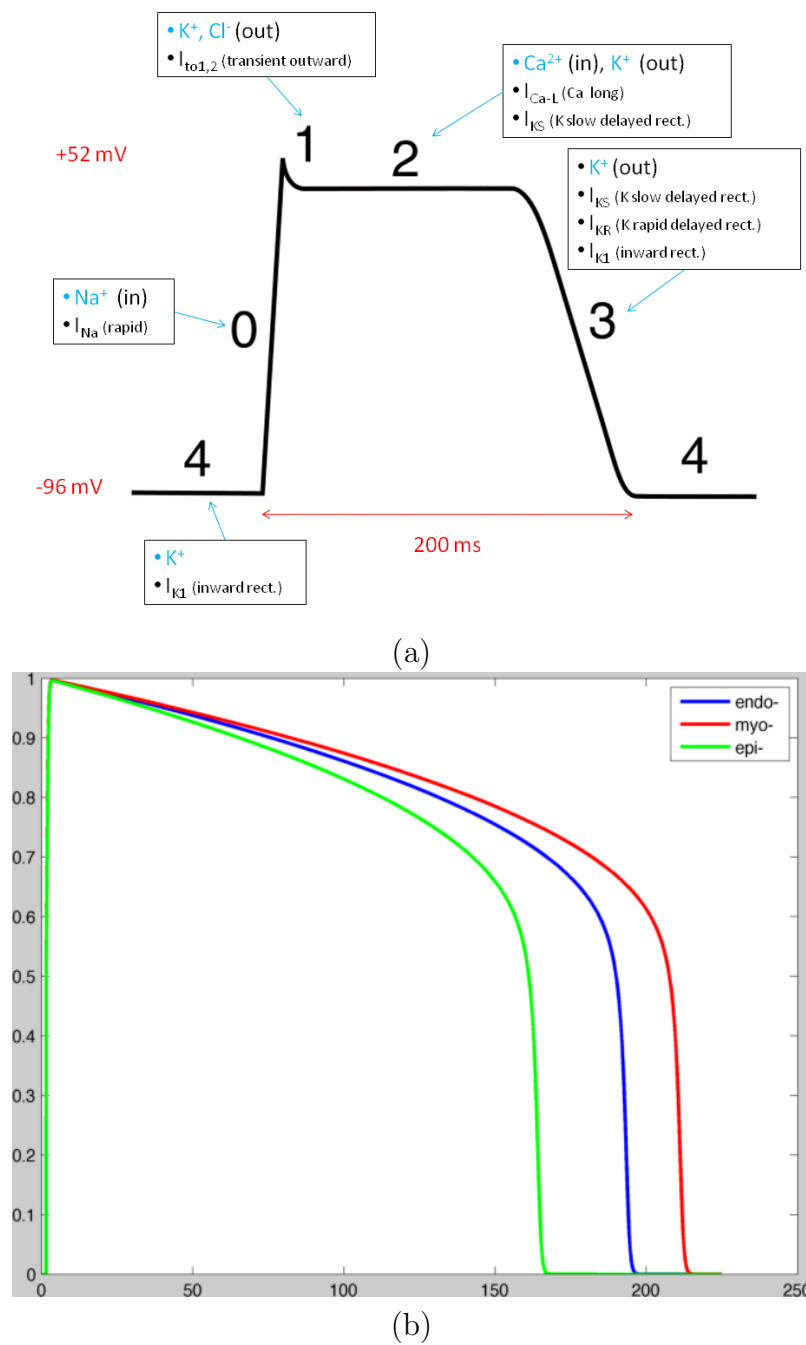


Figure 3.2: Heterogeneity of TMP shapes in endocardium, myocardium and epicardium

activated ion channels in the cell membrane will be activated during the heart motion, which will generate stretch-activated currents [31, 38].

While have realistic simulation results by including stretch-activated currents into the model, the computational cost will increase exponentially. To keep a balance of computational feasibility and physiological meaningfulness of the model, we integrate the first two effects of mechano-electrical feedback into our model. In this way, the electrophysiological model in equation 3.3 can be modified as follows

$$\begin{cases} \frac{\partial V}{\partial t} = \nabla \cdot (\mathbf{D}(\mathbf{F}) \nabla V) + sV(V - a)(1 - V) - VC \\ \frac{\partial C}{\partial t} = -e(C + sV(V - a - 1)) \end{cases} \quad (3.4)$$

Here \mathbf{F} is the deformation gradient tensor obtained from cardiac mechanics. According to the property of deformation gradient tensor, \mathbf{F} can be further decomposed into a rotation matrix \mathbf{R}_{rot} and a stretch matrix \mathbf{S} . The relationship between conductivity tensor \mathbf{D} and \mathbf{F} can be explicitly represented as the following equation

$$\mathbf{D}(\mathbf{F}) = \mathbf{R}_{\text{rot}}^T \mathbf{D}_0 \mathbf{R}_{\text{rot}} \quad (3.5)$$

Thus, the conductivity tensor is changing constantly within a cardiac cycle. In this way, the effect of mechano-electrical feedback caused by the change of fiber orientation is introduced into cardiac electrophysiological model. What's more, the model will be solved in a time-variant computation domain.

3.2.2 Cardiac mechanics

Cardiac mechanics describes the material property of the myocardium and the deformation caused under the loading of internal and external forces. The myocardium is an active nonlinear anisotropic viscoelastic material. Its constitutive law is complex and typically includes an electrical controlled active contractile element and a passive element representing the passive material property [22]. Thus, a simplified mechanical model comprises a TMP controlled active contractile element and a passive parallel element with anisotropic and linear elastic properties is adopted.

Active contractile element

As aforementioned, the processes of active stress generation and cardiac cell shortening occur at the cellular level and depend on the interaction of calcium. Thus, various models on cellular level directly depending on the quantity of calcium have been proposed during the last few decades[6, 47]. These models can reflect realistic ion activities during the heart contraction. However, cellular level models generally need heavy computational cost because of the number of variables and equations need to be solved. To keep a balance of computational feasibility and physiological plausibility, we have selected the ODE-based phenomenological model from [22]

$$\dot{\sigma}_c + \sigma_c = V\sigma_0 \quad (3.6)$$

where σ_c is a scalar related to active stress, and $\dot{\sigma}_c$ is the time derivative of σ_c .

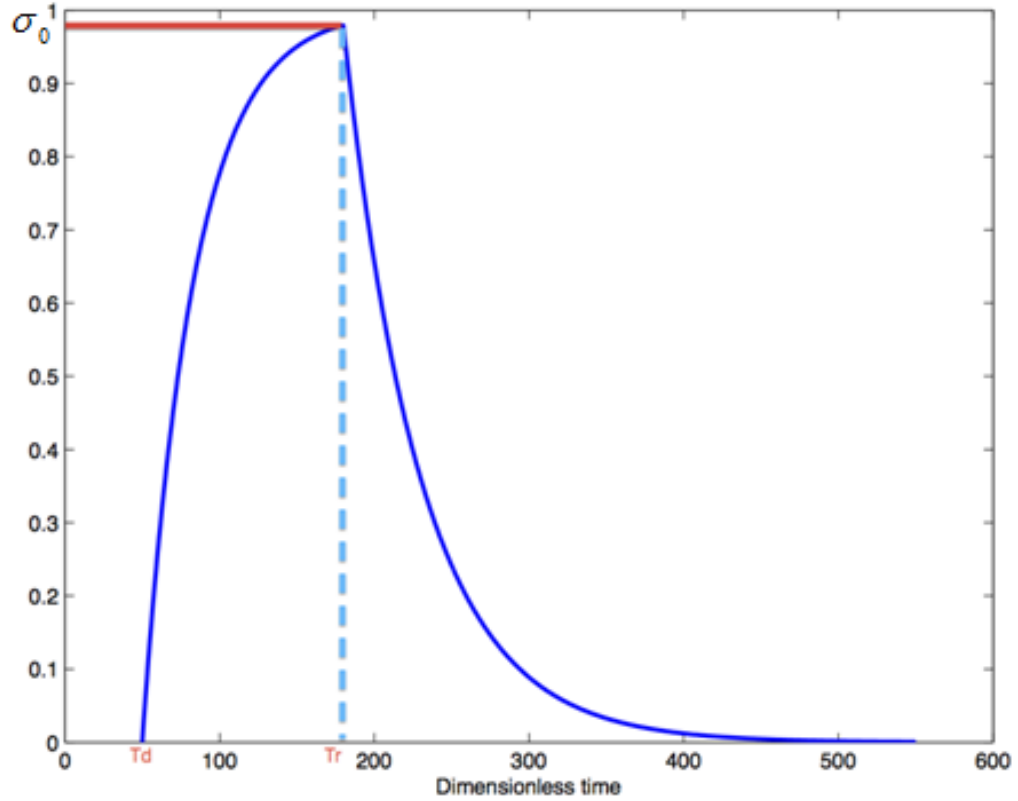


Figure 3.3: Time-vary active stress

σ_0 controls the magnitude of active stress. V is the normalized TMP from 3.15. Through equation 3.6, cardiac electrical activity is coupled to mechanical activity. Because the TMP v is normalized between 0 and 1, and the changes of depolarization and repolarization are abrupt, the analytic solution can be approximated by replacing v with the value of 0 and 1. This makes it possible to avoid the time-stepping of the ordinary differential equation and to directly control the parameters with the following model:

$$\begin{cases} \sigma_c(t) = \sigma_0(1 - e^{\alpha_c(T_d-t)}) & \text{if } T_d \leq t \leq T_r \\ \sigma_c(t) = \sigma_r e^{\alpha_r(T_r-t)} & \text{if } T_r \leq t \leq T_d + HP \end{cases} \quad (3.7)$$

where T_d and T_r are the depolarization and repolarization time, which is depicted as phase 0 and phase 3 in (a) of figure 3.2. HP is the heart period, α_r is the relaxation rate and $\sigma_r = \sigma_c(T_r)$, σ_r and σ_c are introduced for control the decrease and increase of the contraction stress. The shape of the time depended $\sigma_c(t)$ is shown in figure 3.3. In this way, cardiac electrical signal has been coupled with cardiac mechanics. Based on active stress, we can further obtain the contraction Cauchy stress tensor $\boldsymbol{\sigma}$ by:

$$\boldsymbol{\sigma} = -\sigma_c f \otimes f \quad (3.8)$$

where f is the fiber orientation of a point within the computational domain, and \otimes represents the tensor product. The minus sign is necessary because σ_c is always positive while a contraction tensor is required.

Because the total-Lagrangian formulation of cardiac system dynamic will be used in our framework as explained in the section of governing equation of cardiac mechanics, we need further calculate active body and surface forces.

$$R^B = J \text{div}(\sigma_c f \otimes f) \quad (3.9)$$

$$R^S = J\boldsymbol{\sigma}(\mathbf{F}^{-1})^T\mathbf{N} \quad (3.10)$$

where R^B and R^S are body and surface forces, respectively. \mathbf{F} is deformation gradient tensor, J the determinant of \mathbf{F} , and \mathbf{N} is outward normal of the heart surface. For more details on body and surface force calculation, please refer to [48].

Mechanical properties of passive tissue

Since the length of a single cardiac cell changes up to 20% during a heart beat [29], the mechanical analysis should follow finite deformation elasticity theory. Under the assumption that the myocardium is elastic, we can establish the stress-strain relation by Hooke's Law:

$$\mathbf{S} = \mathbb{C}\boldsymbol{\epsilon} \quad (3.11)$$

Here \mathbf{S} is the second Piola-Kirchhoff stress tensor and $\boldsymbol{\epsilon}$ the Green-Lagrangian strain tensor. \mathbb{C} is the elasticity tensor which encodes the material properties of the myocardium. Assume the myocardium material is linear and transversely isotropic, we can obtain the elasticity tensor as follows:

$$\mathbb{C} = \begin{bmatrix} \frac{1}{E_f} & \frac{-v_f}{E_{cf}} & \frac{-v_f}{E_{cf}} & 0 & 0 & 0 \\ \frac{-v_f}{E_{cf}} & \frac{1}{E_f} & \frac{-v_f}{E_{cf}} & 0 & 0 & 0 \\ \frac{-v_f}{E_{cf}} & \frac{-v_f}{E_{cf}} & \frac{1}{E_f} & 0 & 0 & 0 \\ 0 & 0 & 0 & \frac{1}{G} & 0 & 0 \\ 0 & 0 & 0 & 0 & \frac{1}{G} & 0 \\ 0 & 0 & 0 & 0 & 0 & \frac{2(1+v_{cf})}{E_{cf}} \end{bmatrix}^{-1}$$

where E_f , E_{cf} , v_f , and v_{cf} are the Young's moduli and Poisson's ratios along and cross the fiber respectively, $G \approx \frac{E_f}{2(1+v_f)}$ describes the shear property. The Young's moduli describe stiffness, the larger the values, the larger force is needed to make the tissue deform. The poisson's ratios control the incompressibility of the myocardium, range between 0 to 0.5. Unlike isotropic materials, the incompressibility can not be achieved by setting both Poisson's ratios close to 0.5, and numerical tests are required fro a particular problem.

Governing equation of cardiac mechanics

The governing equation of cardiac mechanics describes the balance between external loads from active forces, the kinematic quantities and their internal loads of deformation at any time instant. Following the principle of virtual displacement [49], we can put the active and passive components into the same framework :

$$\int_{t+\Delta t V} ({}^{t+\Delta t}\rho {}^{t+\Delta t}\ddot{u}_i \delta u_i + {}^{t+\Delta t}\tau_{ij} \delta {}_{t+\Delta t}e_{ij}) d{}^{t+\Delta t}V = {}^{t+\Delta t}R \quad (3.12)$$

where

${}^{t+\Delta t}\rho$ = material density of the myocardium at time $t + \Delta t$

${}^{t+\Delta t}\ddot{u}_i$ = components of acceleration vector

${}^{t+\Delta t}\tau_{ij}$ = Cartesian components of the Cauchy stress tensor (forces per unit areas in the deformed geometry)

$\delta {}^{t+\Delta t}e_{ij} = \frac{1}{2}\left(\frac{\partial\delta u_i}{\partial^{t+\Delta t}x_j} + \frac{\partial\delta u_j}{\partial^{t+\Delta t}x_i}\right)$ = strain tensor corresponding to virtual displacements

δu = components of virtual displacement vector imposed on configuration at time $t + \Delta t$, a function of ${}^{t+\Delta t}x_j, j = 1, 2, 3$

${}^{t+\Delta t}x_i$ = Cartesian coordinates of material point at time $t + \Delta t$

${}^{t+\Delta t}V$ = volume at time $t + \Delta t$

and

${}^{t+\Delta t}R = \int_{{}^{t+\Delta t}V} {}^{t+\Delta t}f_i^B \delta u_i d{}^{t+\Delta t}V + \int_{{}^{t+\Delta t}S_f} {}^{t+\Delta t}f_i^S \delta u_i^S d{}^{t+\Delta t}S$ is the external load from active forces

where

${}^{t+\Delta t}f_i^B$ = components of externally applied forces per unit volume at time $t + \Delta t$

${}^{t+\Delta t}f_i^S$ = components of externally applied surface tractions per unit surface area at time $t + \Delta t$

${}^{t+\Delta t}S_f$ = surface at time $t + \Delta t$ on which external tractions are applied

$\delta u_i^S = \delta u_i$ evaluated on the surface ${}^{t+\Delta t}S_f$ (the δu_i components are zero at and corresponding to the prescribed displacements on the surface ${}^{t+\Delta t}S_u$)

By using the total-Lagrangian formulation [49], the equation 3.12 can be represented as:

$$\int_{^0V} (\rho^{t+\Delta t} \ddot{u}_i \delta u_i + {}_0^{t+\Delta t} S_{ij} \delta {}_0^{t+\Delta t} \epsilon_{ij}) d^0V = {}^{t+\Delta t}R \quad (3.13)$$

where 0V and ρ are the volume and material density in the reference configuration. ${}_0^{t+\Delta t} S_{ij}$ are the second Piola-Kirchhoff stress tensor components, and $\delta {}_0^{t+\Delta t} \epsilon_{ij}$ are the Green-Lagrange strain tensor components of the virtual displacements. By using meshfree method [50], equation 3.13 can be converted into matrix formulation as follows (please refer to the appendix for more details):

$${}^t\mathbf{M}^{t+\Delta t} \ddot{\mathbf{U}} + {}^t\mathbf{C}^{t+\Delta t} \dot{\mathbf{U}} + ({}^t\mathbf{K} + {}^t\mathbf{K}_b) \Delta \mathbf{U} = {}^{t+\Delta t}R + {}^tR_b - {}^tR_I \quad (3.14)$$

Variables with superscript t are measured at time t , and variables with superscript $t + \Delta t$ are measured at time $t + \Delta t$. With ${}^t\mathbf{M}$ the mass matrix, ${}^t\mathbf{C}$ is the damping matrix, ${}^t\mathbf{K}$ the stiffness matrix, ${}^t\mathbf{K}_b$ the stiffness matrix from boundary conditions, and ${}^{t+\Delta t} \ddot{\mathbf{U}}$, ${}^{t+\Delta t} \dot{\mathbf{U}}$, $\Delta \mathbf{U}$ are acceleration, velocity and incremental displacement vectors. The vector ${}^{t+\Delta t}R$ is the summation of body and surface active forces, and vector tR_b is external forces from boundary conditions. tR_I is an internal term. By using Newmark method for time integration, the only unknown variable in equation 3.14 is incremental displacement $\Delta \mathbf{U}$.

3.2.3 Cardiac system dynamics

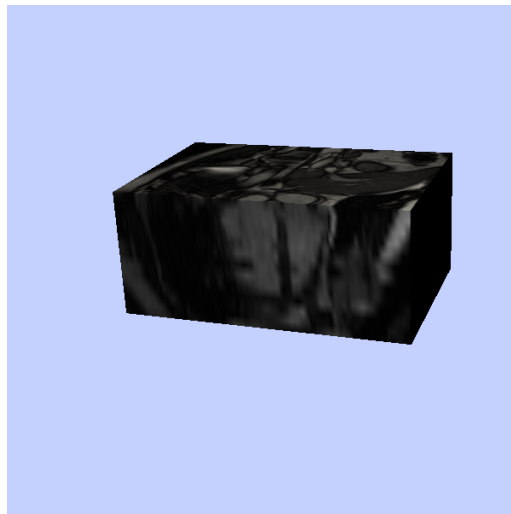
With the explicit formulation of cardiac electrophysiology and mechanics in equations 3.4 and 3.14, we can build the integrated model for cardiac electromechanics:

$$\begin{cases} \frac{\partial V}{\partial t} = -\mathbf{M}_E^{-1}(U)\mathbf{K}_E(U)V + f(V) \\ \mathbf{M}_M\ddot{U} + \mathbf{C}\dot{U} + \mathbf{K}_M\Delta U = R(V) \end{cases} \quad (3.15)$$

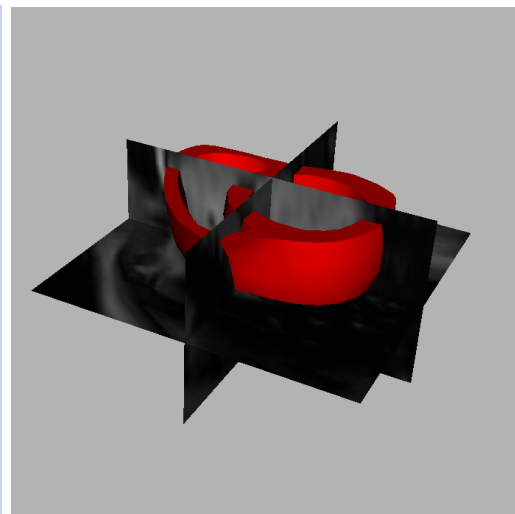
where $(V(x, t), U(x, t))$ characterize the electrical and mechanical properties of point x at time t . Here the variable C in equation 3.3 has been encoded in $f(V)$. The matrices \mathbf{M}_E and \mathbf{K}_E are depended on the displacement vector U because of the effect of mechanoelectrical feedback. The active force vector R is depended on TMP V as in equation 3.9 and 3.10. Thus, cardiac electrophysiology and mechanics are tightly coupled.

3.2.4 Heart representation

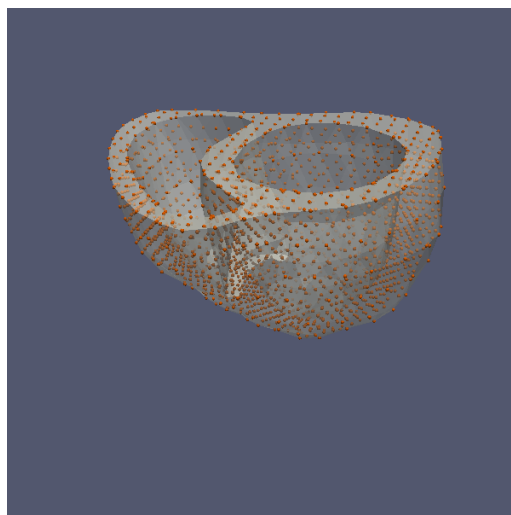
To obtain a realistic simulation of cardiac electromechanics, a subject-specific heart geometry is needed. In figure 3.4, a 3D cardiac MRI image is shown in (a), which includes a subject-specific heart geometry. To automatically segment the heart geometry from the 3D image is not an easy task, because of the complex geometry of the heart and thin walls between the epicardium and the endocardium of the right ventricle. Thus, a lot of automatic image segmentation approaches are not suitable for this specific purpose. In this work, we used a toolkit called CardioViz3D which



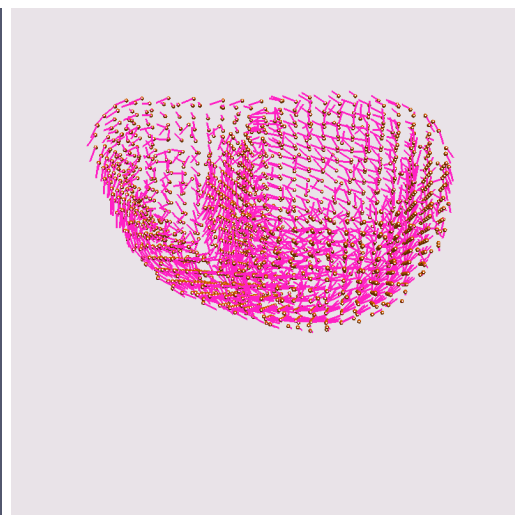
(a) 3D cardiac MR image



(b) cardiac segmentation from 3D image



(c) meshfree particle representation



(d) meshfree particle with fiber directions

Figure 3.4: Meshfree particle representation of the computational domain of the heart

is developed by INRIA group for providing the researcher with a set of tools for pre-processing data and to visualize results of cardiac simulations. The segmentation

result is presented as (b) of figure 3.4.

To numerically implement cardiac system dynamics, equation 3.15, we have to discretize the continuous computational domain. Finite element method is one of the most popular methods for spatial discretization in computational cardiology domain [49]. Nevertheless, its complicated meshing procedures and element-based interpolation functions make the algorithms are either easy to implement but numerically inaccurate or numerically accurate but computationally expensive. We have selected meshfree particle representation approach as shown in (c) of figure 3.4. Meshfree particle representation method is an alternative for finite element method, by using which the computational domain is discretized by a set of unstructured points. As no mesh is required, complicated meshing procedures are excluded, and no re-meshing is needed to improve the spatial discretization accuracy. To consider the anisotropic and inhomogeneous properties of the heart, each point is assigned a fiber direction which was obtained by registrate the subject-specific geometry to a mathematical heart model [51] through non-rigid registration [13].

3.3 Experimental results

3.3.1 Synthetic data

To understand the electromechanically integrated behavior of the model in equation 3.15, simulations on object with simple geometry will be very helpful. In view of this, we conduct our first simulation on a regular cubic object. The object, with its size $60mm*60mm*60mm$, has been utilized to emulate a piece of heart muscle, as shown

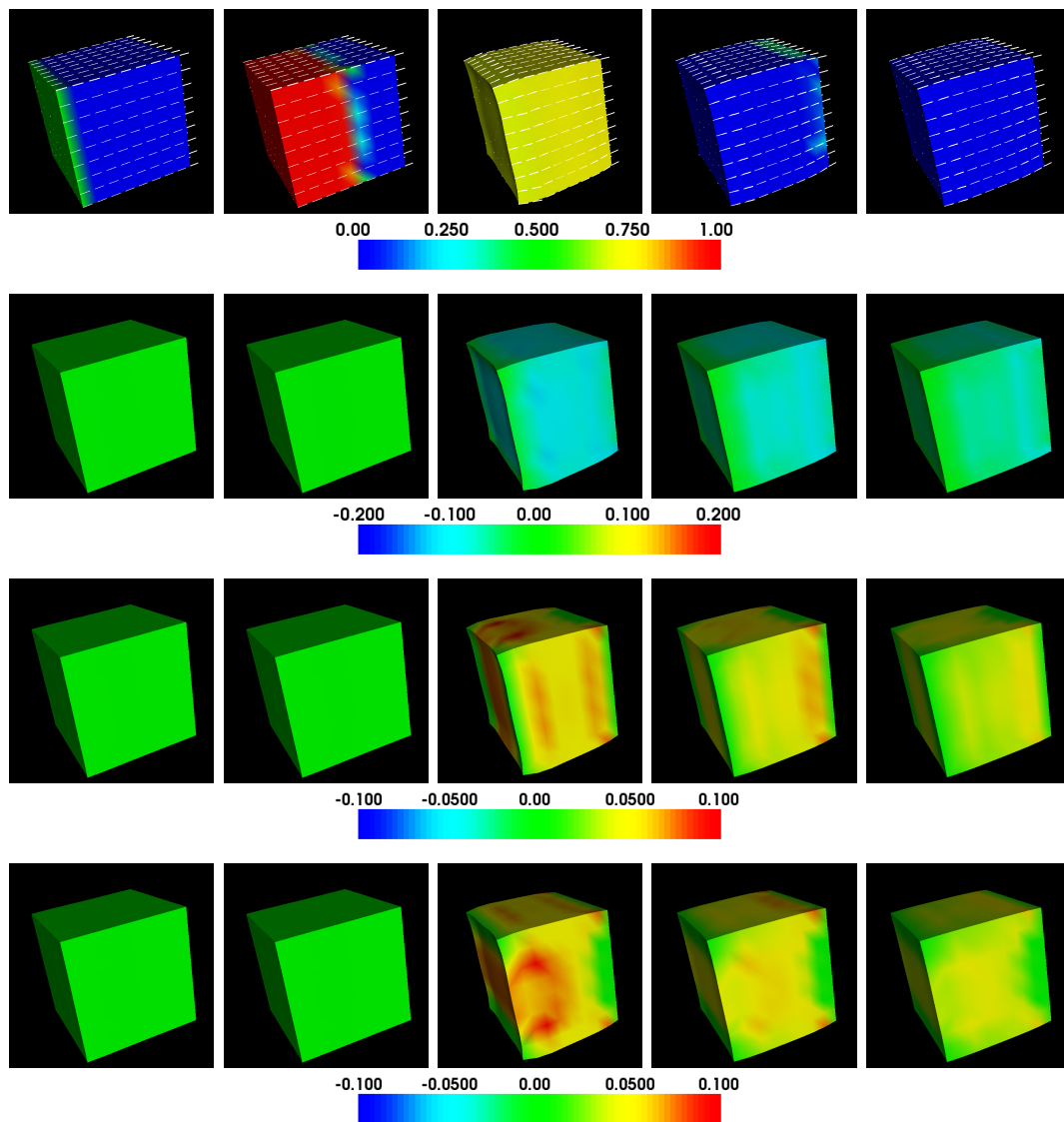


Figure 3.5: Simulation of the proposed heart model on a cubic object. From top row to bottom: electromechanics, strain maps along fiber cross and strain maps along fiber cross. From Left to right with time: 0ms, 13ms, 110ms, 140ms, and 148ms (white lines indicate fiber orientations, the colors represent normalized TMP and strain values.)

in figure 3.5. By using meshfree particle method [52], the cubic object is represented by 729 meshfree particles which are uniformly distributed within the computational domain. The initial fiber orientation of the meshfree particles are pointing towards the right face of the object. To simulate the electromechanical wave propagation, electrical excitation sites are first initiated from the left face which outward normal is in the opposite direction of the fiber orientations. To mimic the physical connection between the object and its surrounding muscle, we limit the movement of the right face.

A cardiac cycle of $200ms$ has been simulated on the object as shown in figure 3.5. To verify the physiological meaningfulness of our simulation, we have presented both electrical and mechanical behaviors of the object in the top row of figure 3.5, which shows the spatiotemporal dynamics of electromechanical wave propagation. After the initial electrical excitation, the electrical wave propagates from the left face to the right face and spreads to the whole object, which follows in a desired pattern. Moreover, we validate the physiological plausibility of the simulation through its mechanical behavior. After a heart cell is electrically excited, under the incompressible material assumption [49], the cell would contract along the fiber direction and extend in fiber cross direction because of the myocardial material property. Thus, the size of the cubic object should be shortened along the fiber direction and extended in fiber cross directions. To show the mechanical behavior of the object, we present the strain maps of the object from row 2 to 4 in figure 3.5. Row 2 lists the strain maps along the fiber direction, the values are almost negative all over the time which means the size of the object is shortening in this direction. This finding is the

same as what we expected that the object contracts along the fiber direction. At the same time, the strain values in both fiber cross directions are positive which means the cube are extending in both two directions as shown in row 3 to 4. These results on simple geometry indicate that our proposed model can provide physiologically meaningful simulations.

3.3.2 Physiological simulation

To further verify the physiological plausibility of the model, we perform simulations on a biventricular heart obtained from University of Auckland [29]. The heart geometry was obtained through experiments on a number of hearts which provide both geometry and their fiber orientations, which is shown as in figure 3.6. Again, based on meshfree particle method, the heart is represented by 2244 meshfree particles with their fiber-sheet-normal directions obtained through interpolation from original data set [51]. To simulate a cardiac cycle, the initial electrical excitation sites need to be determined before setting the simulation. Nevertheless, the realistic Purkinje network of the heart which determines the initial excitation sites is not available, and therefore, we have selected the points on the endocardium and within segments 1, 8, 9 and 15 of the left ventricle as the initial activation sites (according to American Heart Association suggestion, we have divided the left-ventricular myocardium into 17 segments [37] which as shown in figure 3.6) corresponding to the experimental findings by [4], which is shown as in figure 3.7 at time $0ms$. Moreover, we have taken two boundary conditions into account for considering the two phenomena during cardiac cycle: 1) the apex of the heart almost stays still throughout

the cardiac cycle. 2) The base of the heart is constrained by the surrounding myocardium and arteries, which makes it has limited movement along the short axis direction.

Based on the above assumption and conditions, we simulated the electromechanical activity of the heart with cardiac cycle of $500ms$. The simulation results are shown in figure 3.7, which depicts the spread of the electrical wave front from the initial excitation sites throughout the the whole heart along with the heart motion. In this figure, we present four different phases of cardiac cycle. The top row shows the electrical wave quickly propagates from initial excitation sites to the whole hearts which represents the depolarization phase. In the second row, all the myocytes, heart cells, are excited and have very little change in terms of TMP values, which is called "plateau" phase. In the third row, the TMP values quickly drop from the maximum value to the minimum value, which is called repolarization phase. In the bottom row, the electrical signal is almost gone, while the heart is still in relaxation phase. All these phenomena are consistent with a normal heart's behaviors [16], and therefore, validate the physiological plausibility of our model.

Besides the electrical activity, we also validate our simulation through the mechanical behaviors. For a normal heart, the fiber directions in the myocardium are typically perpendicular to the radial direction. As a result, the circumferential strain values are typically negative during the systole phase, and positive during the diastole phase, while the values of radial strain are opposite. In figure 3.8, we present the radial strain maps at different time during the cardiac cycle. In the top row, we can see the strain values are almost zeros which means there is no deformation. This

is because the electrical propagation speed is much faster than mechanical signal, the active forces generated by electrical excitation is still very small at this time (see figure 3.3 for the relationship between the value of active force and time). In the second and third rows, the strain values are greater than zero which means the heart contracts along the radial direction which follows physiological behaviors. In the fourth row, the strain values gradually become smaller and eventually become zero. Besides radial strain maps, we also validate the circumferential strain maps in figure 3.9. As we can see, the circumferential strain values are smaller than zeros through the cardiac cycle, which means the heart muscle is extending in the circumferential directions. All the above findings are consistent with physiological behaviors of the heart [16], which further approve the physiological plausibility of our model.

In the above paragraphs, we have validated our simulation through electrical and mechanical behaviors separately. We further validate its physiological plausibility by checking its electromechanical behaviors. In figure 3.10, we present the simulation results of the curve of volume change curve of the left ventricle and the simulated ECG signal. By comparing with the curves from reference, our simulation can capture the basic pattern of both ECG and ventricular volume change. Because the P-wave is corresponding to the depolarization of the atria and our heart does not include the atria, that is why our simulated ECG shows as flat line. Because we assume the homogeneous property of the heart, the T-wave is simply inverse of the QRS-complex. which can be easily solved by encode inhomogeneity of the excitability on endocardium, myocardium and epicardium.

In cardiovascular physiology, ejection fraction (EF) represents the volumetric

fraction of blood pumped out of the left and right ventricle with each heartbeat or cardiac cycle, which is a very important metric to measure heart failure. The EF value of a normal human being is around 50%. In figure 3.10, we present the volume change curve of left ventricle and show the EF value is 52%. This again shows the physiological meaningfulness of our simulation.

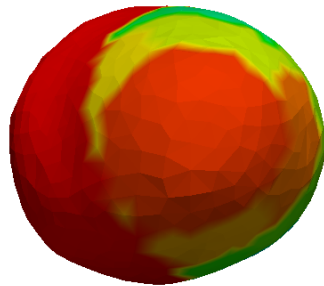
3.3.3 Pathological simulation

Apart from physiological simulations, our model can be used to simulate the heart under pathological conditions. In this work, we present simulation results under two conditions: left ventricular bundle block (LBBB) and cardiac infarction.

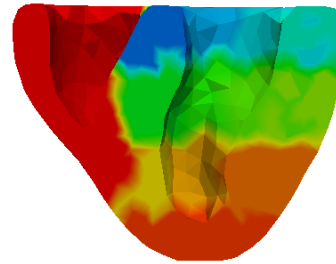
In normal condition, the electrical activation progresses from the endocardium to the epicardium simultaneously in both left and right ventricle. LBBB is a condition in which there is a delay or obstruction along the pathway that electrical impulses travel to the left ventricle to make you heart beat. In that way, the electrical activation progress on the right ventricle will be earlier than the left ventricle. To simulate this condition, we removed the initial excitation sites on the endocardium of the left ventricle as shown in figure 3.11. As we can see, one significant difference from simulation results under normal condition, as in figure 3.7, is the electrical wave propagation is asynchronized in left and right ventricle, which propagates from the right ventricle to the left ventricle. To further show the difference between the simulations under normal condition and LBBB, we make a comparison between the volume change curve of the two conditions as in figure 3.12. We find there is a delay for the simulation of LBBB condition to reach the minimum volume. However, the

pattern and range of volume change does not change.

We also simulate the cardiac cycle under myocardium infarction as in figure 3.13. In this simulation, we assume segments 5 and 6 are not electrically excitable. As we can see, the electrical wave propagates from the initial excitation sites through the heart except the infarcted regions. To compare the simulation with normal condition, we plot the left ventricle volume change curve in 3.14. We found the left ventricle gets to the minimum volume earlier than the normal condition, which means its repolarization phase earlier than normal condition. We also find that the the minimum volume of the left ventricle is greater than the normal condition, which means the infarction affects the heart contraction ability. This can also found from figure 3.3.3, the heart has very limited contraction in the infarcted area.

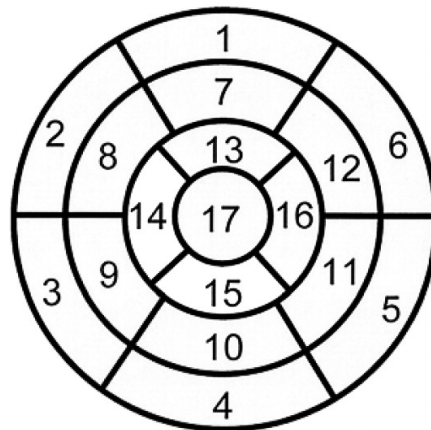


(a) Bulleye view of 17 segments of the left ventricle and along with right ventricle



(b) Inside view of 17 segments of the left ventricle and along with right ventricle

Left Ventricular Segmentation



- | | | |
|------------------------|-----------------------|---------------------|
| 1. basal anterior | 7. mid anterior | 13. apical anterior |
| 2. basal anteroseptal | 8. mid anteroseptal | 14. apical septal |
| 3. basal inferoseptal | 9. mid inferoseptal | 15. apical inferior |
| 4. basal inferior | 10. mid inferior | 16. apical lateral |
| 5. basal inferolateral | 11. mid inferolateral | 17. apex |
| 6. basal anterolateral | 12. mid anterolateral | |

(c) AHA 17 segments

Figure 3.6: The 17 segments and the nomenclature of the left-ventricular myocardium recommended by the American Heart Association, shown on a circumferential polar plot [37]

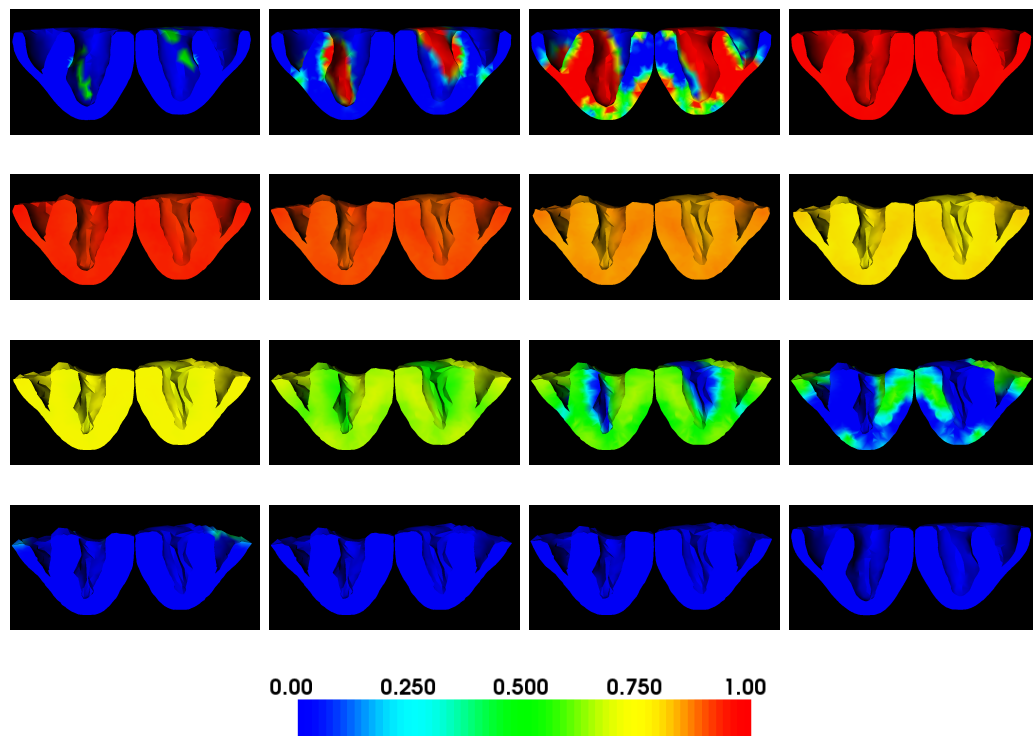


Figure 3.7: Simulation of cardiac electromechanics. the color indicates normalized TMP. From left to right and top to bottom. The time for the snapshots are at 0ms, 5ms, 10ms, 20ms, 40ms, 55ms, 75ms, 95ms, 110ms, 125ms, 130ms, 135ms, 140ms, 145ms, 195ms, 430ms

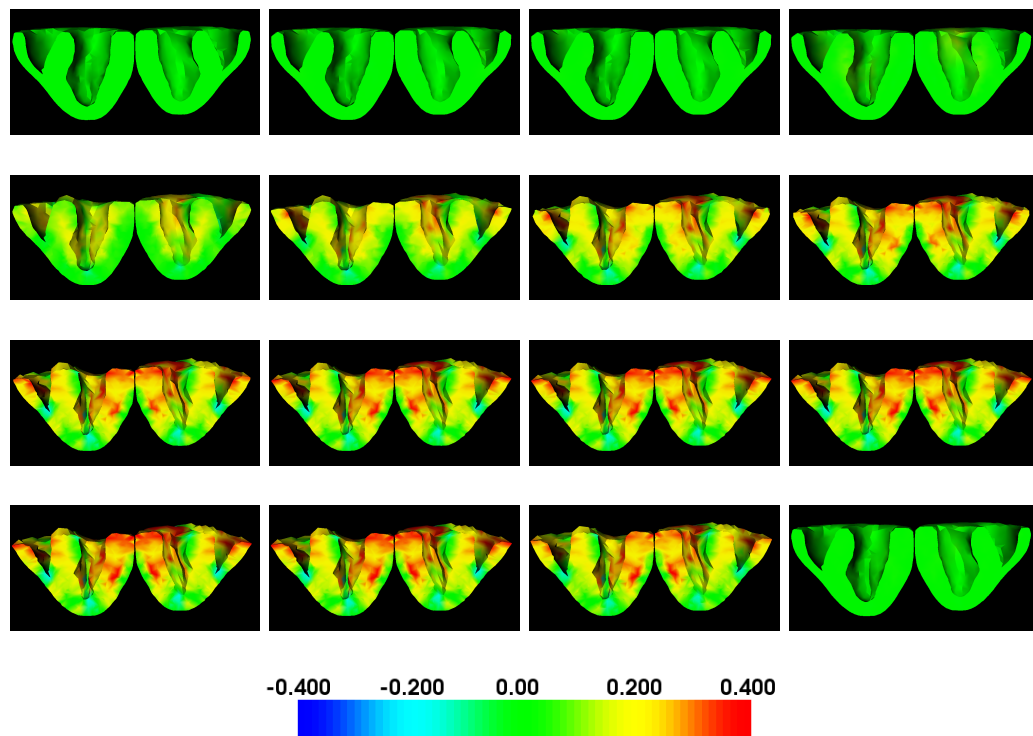


Figure 3.8: Radial strain maps. The time for the snapshots are at 0ms, 5ms, 10ms, 20ms, 40ms, 55ms, 75ms, 95ms, 110ms, 125ms, 130ms, 135ms, 140ms, 145ms, 195ms, 430ms

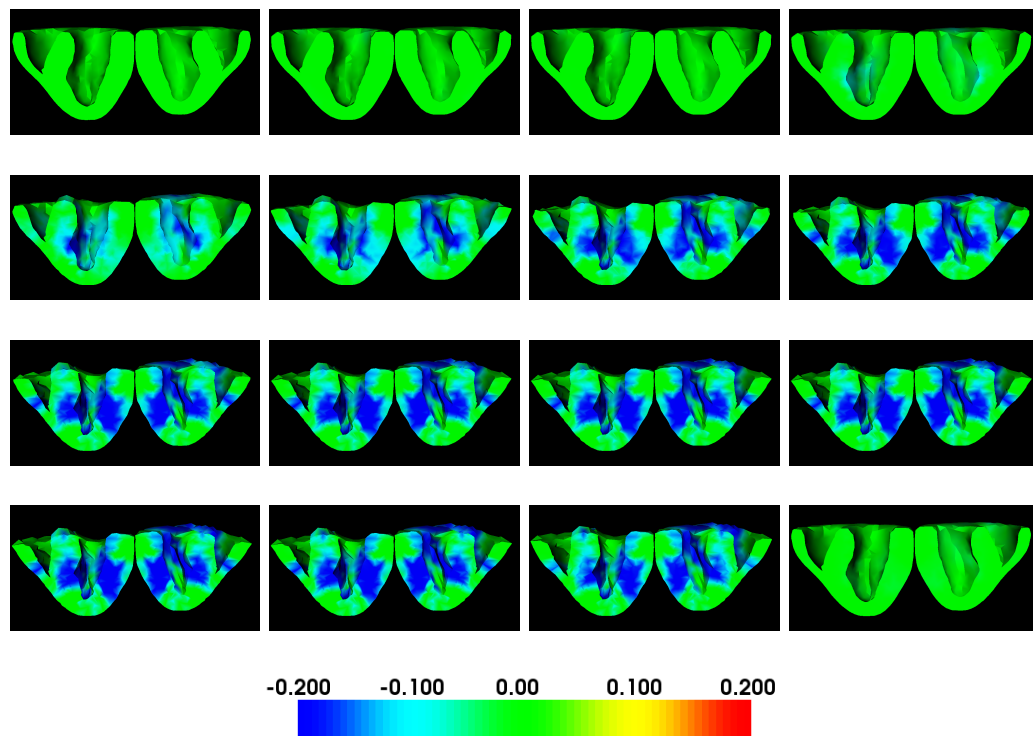
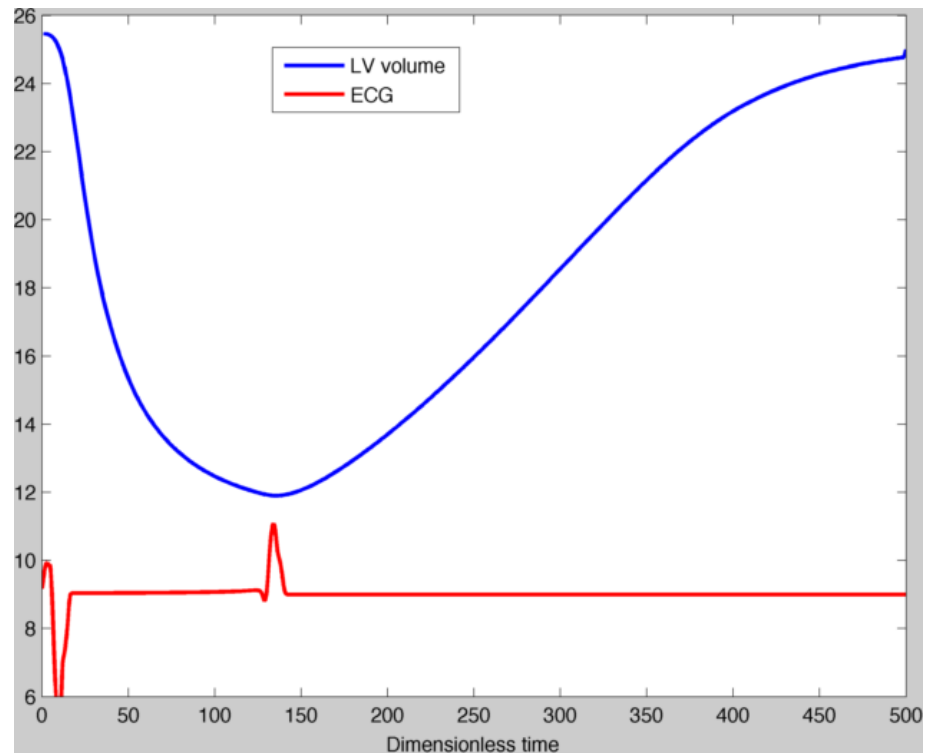
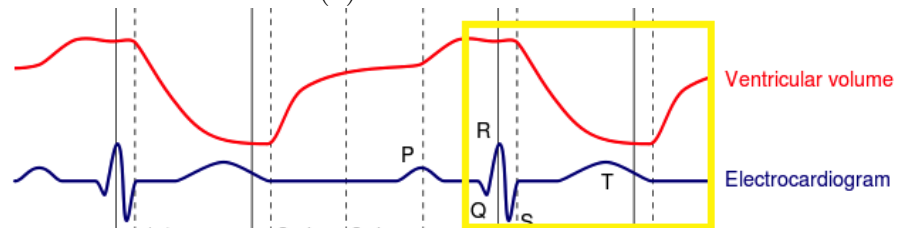


Figure 3.9: Circumferential strain maps. The time for the snapshots are at 0ms, 5ms, 10ms, 20ms, 40ms, 55ms, 75ms, 95ms, 110ms, 125ms, 130ms, 135ms, 140ms, 145ms, 195ms, 430ms



(a) Simulation results



(b) Reference curves from [53]

Figure 3.10: Comparison between simulation results of left ventricle volume change curve and single-lead ECG

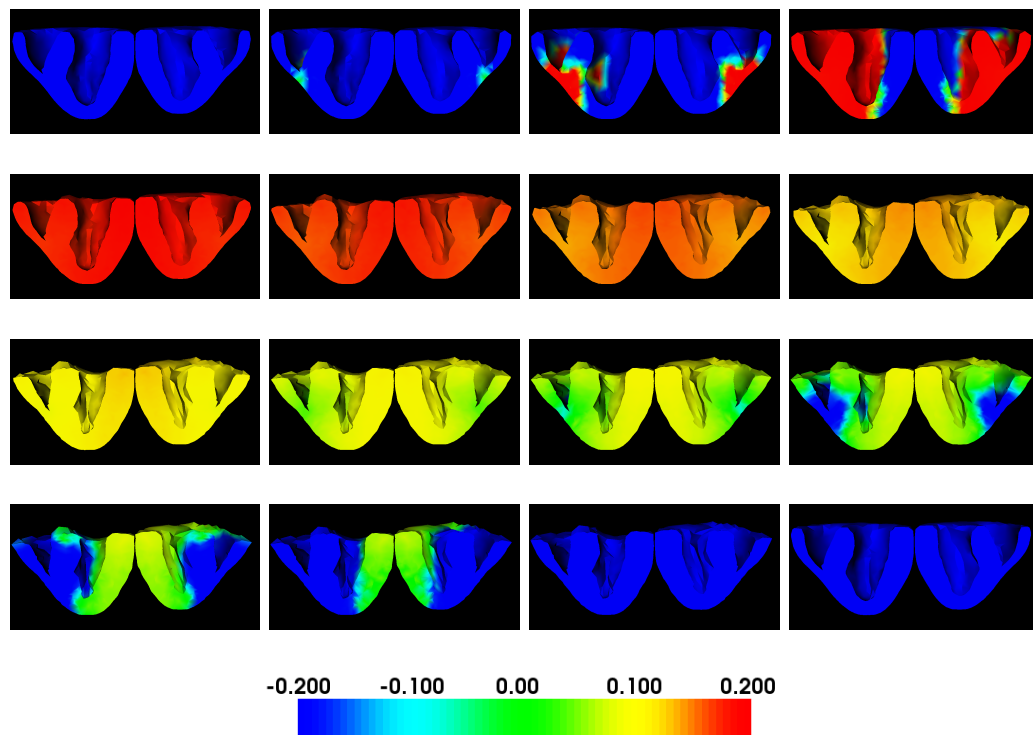


Figure 3.11: Simulation of LBBB

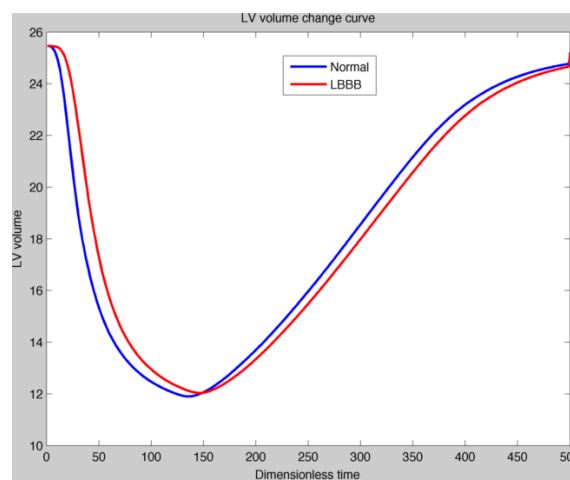


Figure 3.12: Cardiac cycle simulation under LBBB condition. The time for the snapshots are at 0ms, 5ms, 10ms, 20ms, 40ms, 55ms, 75ms, 95ms, 110ms, 125ms, 130ms, 135ms, 140ms, 145ms, 195ms, 430ms

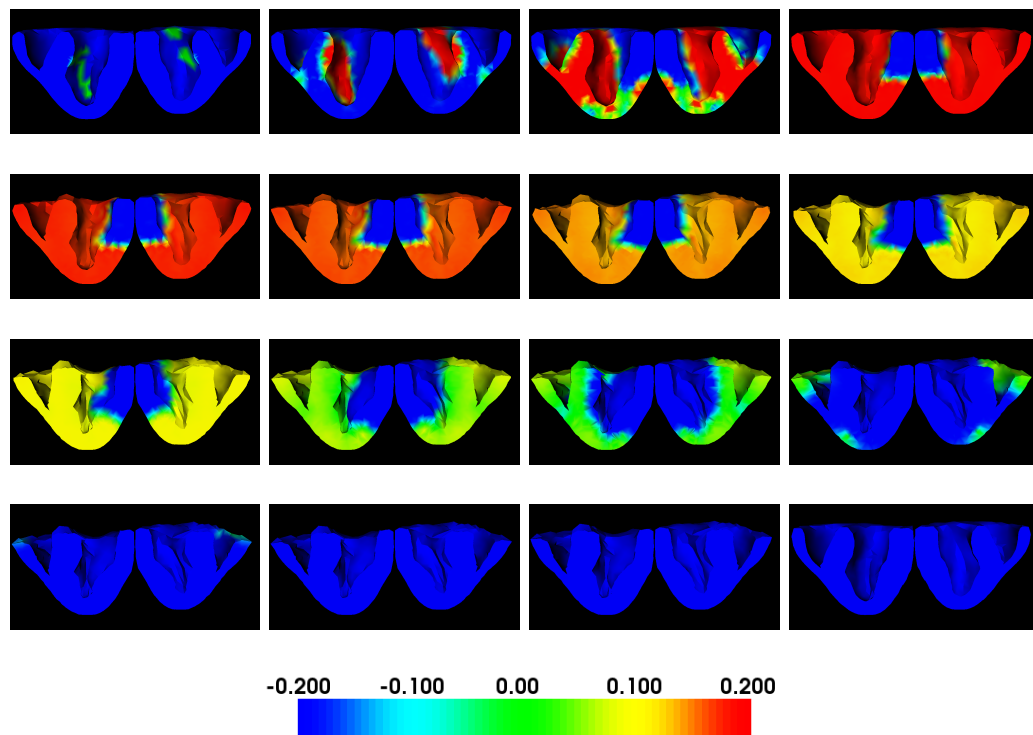


Figure 3.13: Simulation under myocardium infarction. The time for the snapshots are at 0ms, 5ms, 10ms, 20ms, 40ms, 55ms, 75ms, 95ms, 110ms, 125ms, 130ms, 135ms, 140ms, 145ms, 195ms, 430ms

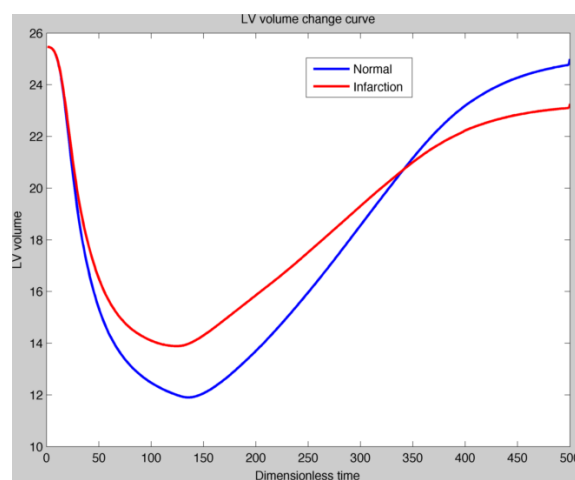


Figure 3.14: Cardiac cycle simulation under myocardium infarction condition

Chapter 4

The effect of cardiac motion on noninvasive transmural imaging of cardiac electrophysiology

4.1 Introduction

Noninvasive transmural imaging of cardiac electrophysiology aims to quantitative interpretation of the 3D electrical activity of the heart based on noninvasive electrophysiological data, such as ECG or body surface potential maps (BSPMs). In the last decade, several studies have been demonstrated that noninvasive transmural imaging technique can be successfully applied to reconstruction of the healthy and abnormal electrical activities of the heart [54, 55, 26, 7, 24], and which has the potential for assisting the doctors with heart diagnosis. Although the results were

promising, they were all based on the assumption that the heart geometry is fixed during the cardiac cycle. In other words, the mechanical activity, such as the motion and twist, of the heart were completely ignored. Nevertheless, the heart is an electromechanical organ that exhibits both electrical and mechanical activities. Thus, this assumption has two shortcomings that limit their practical applications. First, it introduces geometry errors during the computation because the heart is moving constantly and thus the relative position between the torso and heart is changing constantly. Second, it is not feasible to reveal the mechanisms behind some pathological activities that need considering both electrical and mechanical activities, such as heart failure and ventricular desynchronization. To overcome the first limitation, some researchers have been investigating the potential numerical errors introduced by ignoring the mechanical activity through shifting the global position or orientation of the heart [34, 33, 32]. However, the global position or orientation change of the heart cannot reflect the realistic heart motion. Thus, a more efficient and accurate approach for understanding the effect of cardiac motion on noninvasive estimation of cardiac electrophysiology is needed. What's more, all the existing works were focusing on studying the motion effect on reconstruction of the epicardial electrical activity rather than transmural electrical activity. Compared to the electrical activities on the epicardium, transmural electrical activity of the heart can directly and precisely reflect the location and extent of abnormal regions in the heart which can advance the methods with understanding the epicardial electrical activity only. As a result, noninvasive transmural imaging of cardiac electrophysiology has been great of interest among cardiac research communities [54, 55, 26, 7, 24]. However,

to the best of our knowledge, this is the first work to study the effect of cardiac motion on noninvasive transmural imaging of cardiac electrophysiology.

In the previous chapter, we proposed a biologically-inspired mathematical model for simulation of cardiac electromechanics. Due to its electromechanically integrated property, it can be naturally served as a central role for reconstruction of transmural cardiac electrophysiology from BSPMs and taking into the effect of cardiac motion at the same time. Based on this observation, we utilize the proposed heart model to generate realistic heart simulation which includes electrical activity, mechanical activity and their interactions. To this end, we first build a forward relationship between the spatiotemporal dynamics of volumetric cardiac electrophysiology (TMP) and BSPMs. Then, we solve an inverse problem to estimate the volumetric TMP based on the given BSPMs through an optimization approach. Nevertheless, the inverse problem is typically an ill-posed problem, which means the solution may not be unique and also a small change on the value of BSPMs may have a huge effect to the TMP values. To tackle this problem, we solve the optimization approach by adding a regularization term to narrow the solution space. More details on solving the forward and inverse problems will be introduced in the following sections.

4.2 Forward problem

4.2.1 Coupled heart-torso representation

To build a relationship between volumetric TMP and BSPMs, we need to establish a geometrical alignment between the heart and the torso. Thanks to the advanced

medical imaging techniques, the torso can be extracted through segmenting of 3D MR or CT images as shown in (a) of figure 4.1. In a similar way, the heart geometry can also be extracted from medical images. Before conducting any computational operations, we need to discretize the computational domain, which are the heart and the torso in our problem. Due to the large volume and relative homogeneity properties of the torso, we use boundary-element method to discretize the torso by which the torso is represented by a graph of connected triangles as shown in (b) of figure 4.1. As aforementioned, the computational domain of the heart is represented by using meshfree particles method as shown in (c) of figure 4.1. The relative position of the heart and torso can be determined through image registration based on some landmarks, such as the apex and epicardium of the heart. After these steps, a coupled heart-torso geometry can be built which is shown as (d) of figure 4.1.

4.2.2 TMPs-to-BSPMs mapping

Due to the relatively low frequencies in the ECG signals, the quasi-static approximation of Maxwell's equations can be used to describe how cardiac electrical sources generate the potential distributions on the body surface [56]. Following this idea, a relationship between volumetric TMP distribution and BSPMs distribution can be established as follows

$$\nabla \cdot (\sigma \nabla \phi) = \nabla \cdot (-\mathbf{D}_h \nabla v) \quad (4.1)$$

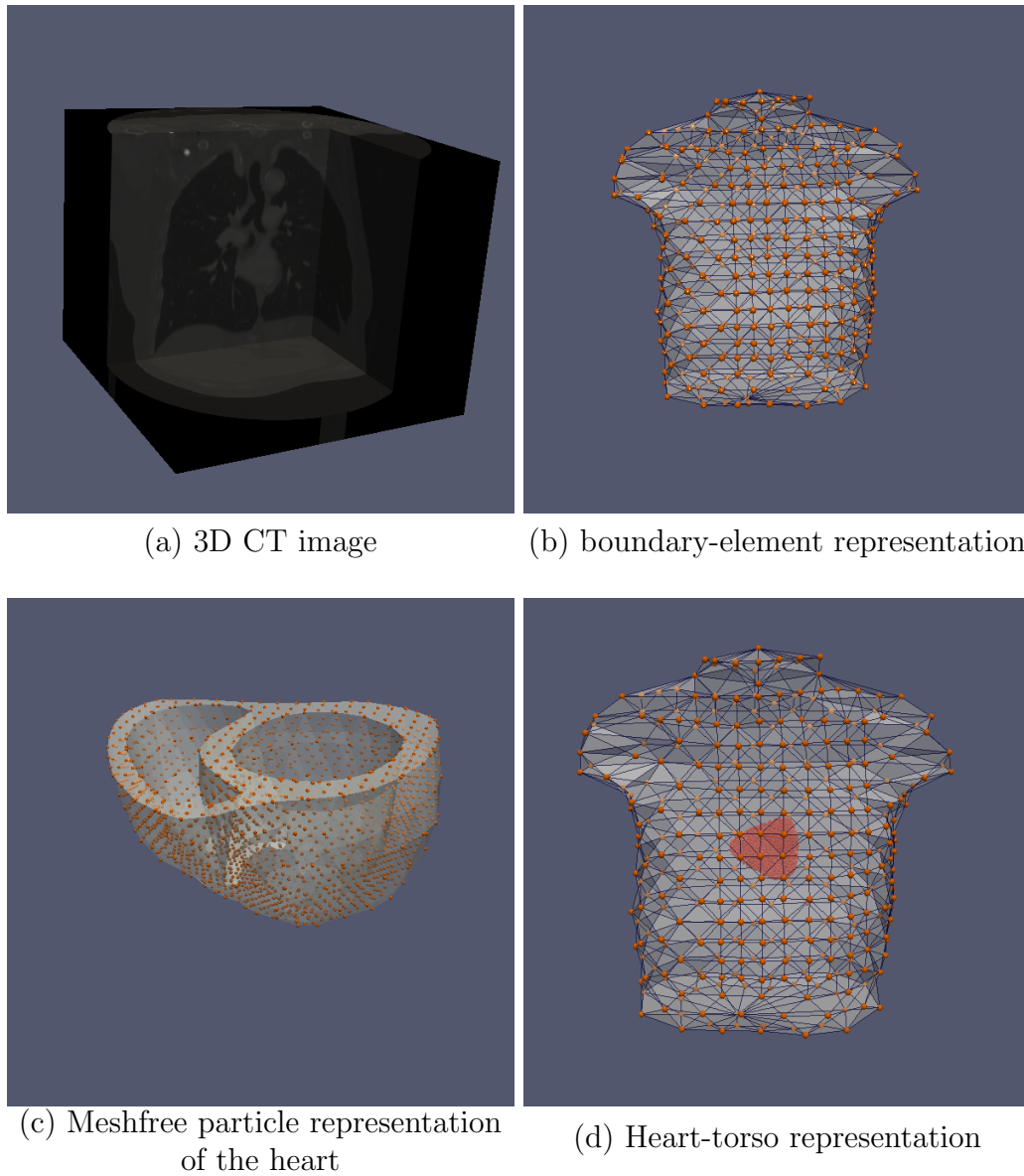


Figure 4.1: Meshfree-BEM representation of the heart-torso structure

where ϕ and v stand for BSPMs and TMP respectively, and σ , \mathbf{D}_h represent torso and intercellular conductivities, respectively.

With meshfree-BEM representation of the heart-torso structure, equation 4.1

can be further converted into a time-variant linear equation

$$\Phi(t) = \mathbf{H}_{\mathbf{E}}(t)V(t) \quad (4.2)$$

where vector $\Phi(t)$ and vector $V(t)$ represent the potential distribution on the body surface and TMP within the myocardium at time t , respectively. Here $\mathbf{H}_{\mathbf{E}}(t)$ is a transfer matrix reflects the linear relationship between TMP and BSPMs. Unlike conventional approaches [56, 54, 55] where the transfer matrix is fixed during the cardiac cycle, it is a time-variant variable here because of the incorporating of the cardiac motion. what's more, $\mathbf{H}_{\mathbf{E}}(t)$ also encodes all the structural and conductivity information of the heart-torso structure.

4.3 Inverse problem

The reconstruction of transmural cardiac electrophysiology from BSPMs is equivalent to finding an optimal $V(t)$ given $\mathbf{H}_{\mathbf{E}}(t)$ and $\Phi(t)$ in equation 4.2. It is an inverse problem and is unfortunately ill-posed. Small measurement errors in the BSPMs $\Phi(t)$, or any geometrical errors encoded in the transfer matrix $H_e(t)$ can lead to large unbounded errors [34]. To tackle this issue, we reformat the problem into an object function minimization problem

$$\min_{V(t)} \|\Phi(t) - \mathbf{H}_{\mathbf{E}}(t)V(t)\|^2 + \lambda C(V(t)) \quad (4.3)$$

where the first term is a data fidelity term that enforcing the relationship between TMP and BSPMs in equation 4.2, and the second term is a regularization term which enforces the smoothness of TMP distribution within the 3D myocardium. The regularization term can be either L_1 norm or L_2 norm. λ is a constant, weighting parameter that keeps a balance between the data fidelity term and data smoothness term. In the recent studies, total variation method shows better performance than other regularization methods in noninvasive cardiac electrophysiology estimation [54]. Thus, to estimate transmural TMP from BSPMs, we select the total variation regularization to tackle the ill-posed problem in equation 5.7. Thus, our problem becomes to find an optimal solution for the following equation

$$\min_{V(t)} \|\Phi(t) - \mathbf{H}_E(t)V(t)\|^2 + \lambda\|\nabla V(t)\| \quad (4.4)$$

where ∇ is the spatial derivative along x, y and z axes. λ is determined by the experiments. In this work, the value is $1e - 4$ for all the experiments. To solve the equation, we adopt an open source software CVX which was written in Matlab [?].

4.4 Experimental results

4.4.1 The effect of cardiac motion on the forward problem

Before we investigate the effect of cardiac motion on the inverse problem of cardiac electrophysiology, it is critical for us to understand the effect of cardiac motion on the forward problem, which we conduct experiments through two difference perspectives:

cardiac cycle simulation and standard 12-lead ECG signal simulation.

Cardiac cycle simulation

In this study, mathematical simulation has been conducted on a biventricular heart with realistic geometry. The geometry of the heart is extracted from MRI images as in (c) of figure 4.1, which is publicly downloadable [57]. After image segmentation slice by slice and 3D surface mesh generation, the heart can be represented by 2017 meshfree particles bounded by the surface mesh. Since the ventricular conduction system is not available for the current heart, the initial activation sites are selected according to the experimental study from [4]. These initial activation sites will be considered as the initial condition for the forward simulation.

In figure 4.2, we make a comparison between simulation results of our model and an electrophysiological model with fixed heart geometry. We find there are two major differences between these two simulations: first, the simulation provided by our model presents both electrical and mechanical activities, while the electrophysiological model with fixed geometry only can show the electrical activity. Thanks to the electromechanical coupling property of the model. Second, the action potential duration (APD), which is the time period between ventricle depolarization and ventricle repolarization, of our model is slightly shorter than the model with fixed geometry. As we can see the results at time 255 ms, TMP values of some areas on the endocardium are close to zero in the simulation by our model, while the values in the simulation by using static heart model are greater than zero in the same areas. This indicates the repolarization time of our model is earlier than static heart

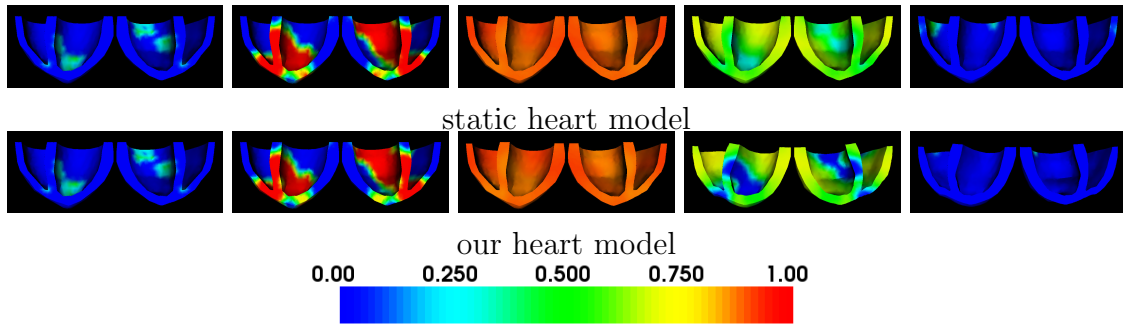


Figure 4.2: Simulation results comparison between static heart model and our electromechanical model. left to right with time, 1 ms, 18 ms, 72 ms, 255 ms, and 288ms. The color indicates normalized TMP values

model. Considering the depolarization time of both models are almost the same, thus the APD of our model is shorter than static heart model. The main reason of APD shortening is the fiber shortening during heart contraction. This simulation result is consistent with what found in the work [58], in which the authors used a cellular level electromechanical coupled heart model to simulate ECG in two dimensional space and found that electromechanical coupled heart model can shorten APD compared to a static heart model.

12-lead ECG simulation

We also investigate the effect of cardiac motion on the forward cardiac electrophysiological problem through simulation of standard 12-lead ECG. For ECG simulation, we obtain the heart geometry, fiber orientation and torso geometry from the publicly available database [57]. By using meshfree-BEM method, the heart-torso structure can be represented as in Figure 4.1 (d). The initial activation sites are some regions on the endocardium according to the experimental study from [4].

Figure 4.3 depicts normal 12-lead ECG simulation by both static heart model and our electromechanical model. Compared to a real ECG, we can find that the waves of our model (in red) have a correct orientation in each of the 12 leads. Because we utilized normalized TMP value instead of values in the physiological range, our simulation are not able to provide the quantitative ECG amplitude in physiological range but it can describe the ECG patterns correctly. We also compare them with the results of static heart model, and find the results of these two models are very similar except the amplitude of T-wave. The T-wave amplitude of our model is larger than a static heart model, because the heart has the maximum contraction at the T-wave, and the relative distance between heart and torso is also maximized at T-wave. This finding is also consistent with the existing works [58, 33, 28]

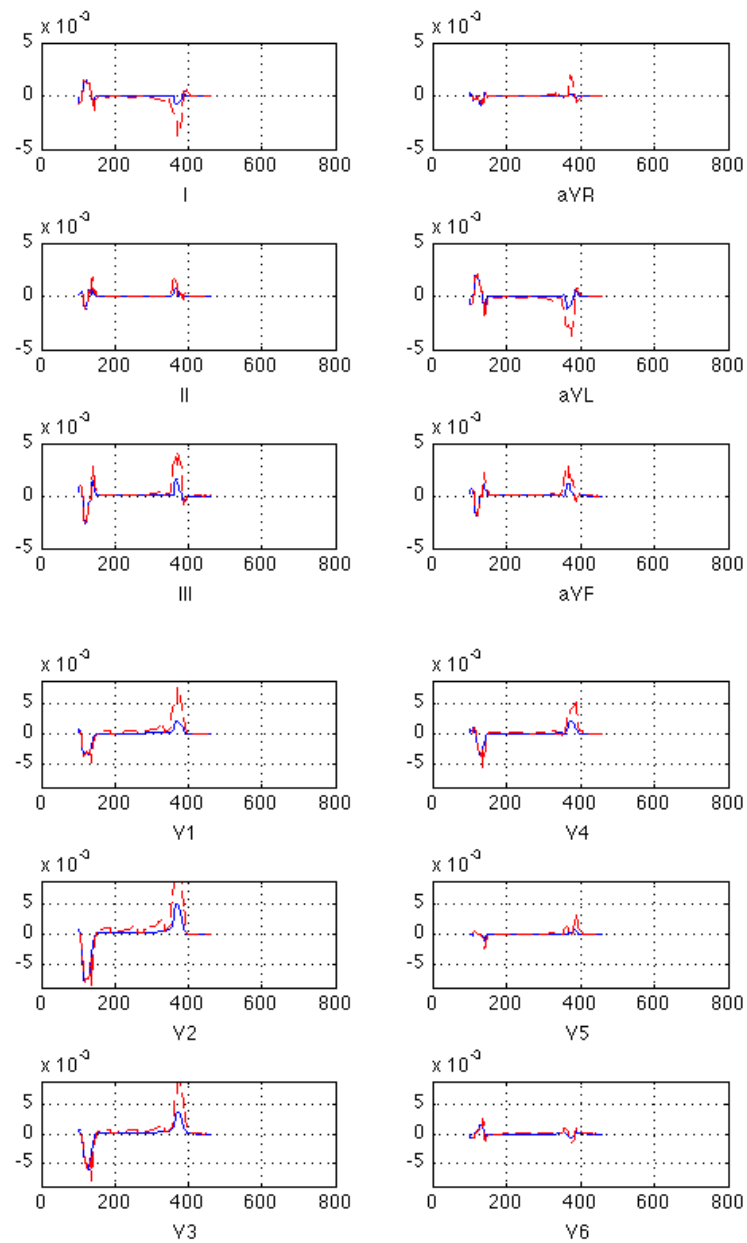


Figure 4.3: Normal 12-lead ECG simulation, blue: static heart model; red: our proposed heart model

4.4.2 The effect of cardiac motion on the inverse problem

To study the effect of cardiac motion on the inverse problem, we conduct a set of synthetic experiments on an image-derived heart-torso model. The heart is represented by 2244 points by using meshfree method, and the torso is represented by 3760 points with boundary element method. A coupled heart torso structure can be found in figure 4.1.

We investigate the effect of cardiac motion to noninvasive transmural imaging of cardiac electrophysiology under two different conditions: healthy and post-myocardium infarction. For each condition, a simulation of cardiac cycle with duration 500 ms was conducted (because the P-wave is absent, the cardiac cycle is shorter than regular cardiac cycle). With the forward mapping, we can record the BSPMs simultaneously, which will be utilized as the inputs for the inverse problem. In figure 4.4, we present an example of volumetric TMP distribution and associated BSPMs in figure 4.4.

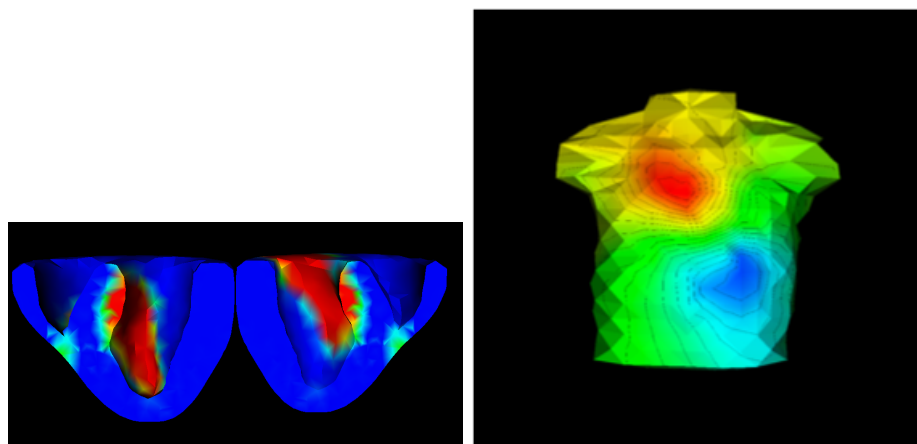
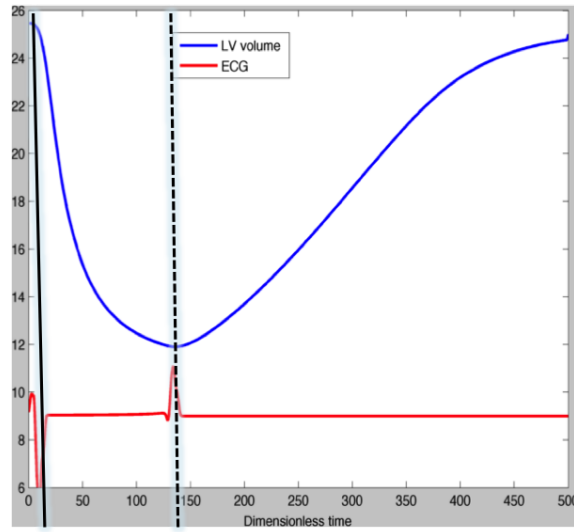


Figure 4.4: left: TMP; right: BSPMs

To mimic the noise in real signal, we add different levels of gaussian noise to the simulated BSPMs and obtained four groups BSPMs with signal to noise ratio (SNR) 20db, 30db, 40db and 50db. The noise-corrupted BSPMs will be used as the measurements for TMP reconstruction.



(c) TMP reconstruction with fixed geometry

Figure 4.5: TMP reconstruction on a normal heart. From left to right, the first three columns are at depolarization phase, the last two columns are at repolarization phase

In figure 4.5, we present the volume change of the left ventricle and lead I ECG signal. As we can see, the heart barely has contraction at the beginning of the cycle, and has the largest contraction at the time around 130ms. To understand the effect of cardiac motion on cardiac electrophysiology, we select the heart geometry at two different time stamp: the geometry at 10 ms and 130 ms after the onset of the ventricular depolarization. Due to the ill-posedness property of the inverse problem, the solution of equation 5.7 is not necessary in the same range as the original values.

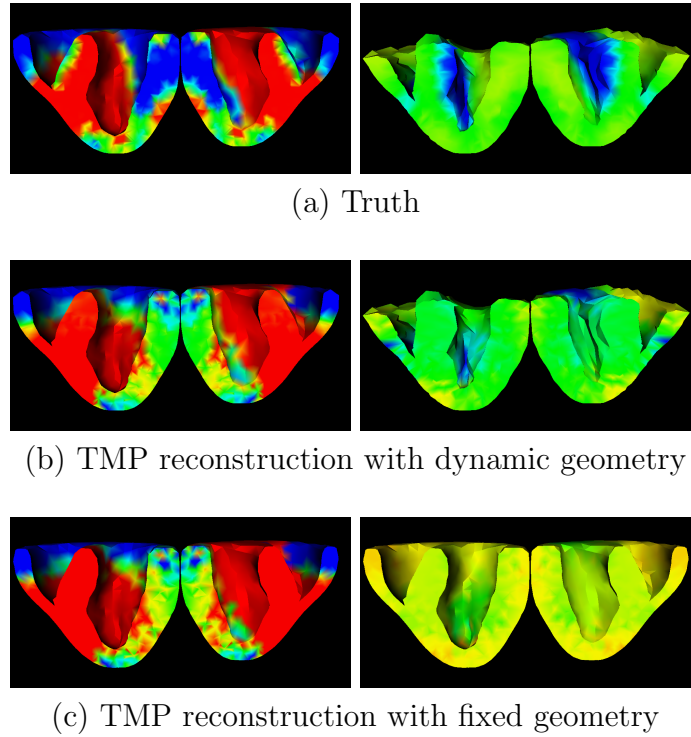


Figure 4.6: TMP reconstruction at different time. Left: 10ms after the onsite of ventricular depolarization; Right: 130ms after the onsite of ventricular depolarization. The colors are manually tuned to have a good visual comparison, they only reflect the pattern of the TMP distribution but not the true value

Thus, we use *correlation coefficient* (CC) to measure the similarity of estimated TMP value and the ground truth:

$$CC = \frac{\sum_i^n [(v_t)_i - v_t^*][(v_g)_i - v_g^*]}{\|v_t - v_t^*\|_2 \|v_g - v_g^*\|_2} \quad (4.5)$$

Healthy heart

In figure 4.6, we listed the results of TMP reconstruction of a healthy heart with and without integrating cardiac motion. The top row shows the simulation results of our

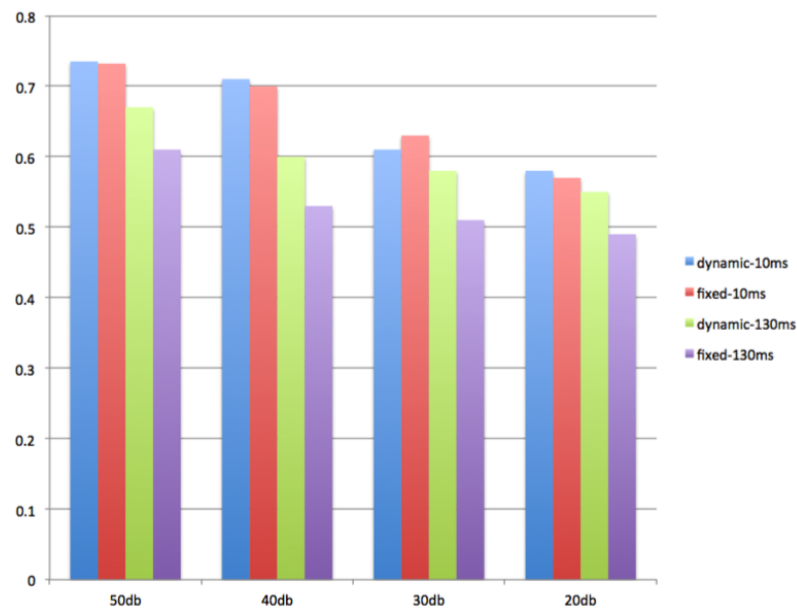


Figure 4.7: Statistical analysis of noninvasive transmural imaging accuracy on healthy heart based on correlation coefficient

heart model, which can be considered as ground truth. The middle and bottom row list the reconstruction results with and without integrating cardiac motion. From visual perspective, the TMP patterns are quite similar at the left column, and are different at the right column. That's because the heart is in depolarization phase at the left column which has very limited deformation, and therefore there is very little motion effect. However, the heart has large deformation at repolarization phase as listed in the right column. The reconstruction results with dynamic geometry gets more accurate results compared to the one with fixed geometry.

We further present the statistical analysis, CC value between estimated TMP and simulated ground truth, for the heart under healthy condition in figure 4.7. In the figure, we present the reconstructed results with different levels of noise in

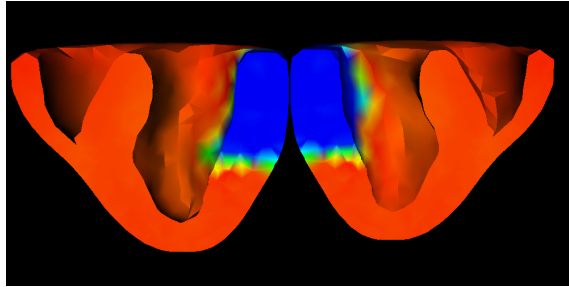


Figure 4.8: The heart with post-myocardium infarction. Blue: infarcted region; red: normal region

BSPMs. Overall, the CC values between the reconstruction with fixed geometry and dynamic geometry are quite close at time 10ms. That's because the heart has very little deformation in the dynamic heart model. Nevertheless, the estimated TMP with dynamic heart model are consistent accurate then the ones estimated with static heart model. That's because the heart has large deformation at that time. Estimation of the TMP by using static heart geometry introduced large geometrical errors. At last but not least, the CC values are decreasing when the SNR are decreasing.

Post-myocardial infarction

Besides the healthy condition, we also investigate the effect of cardiac motion on noninvasive transmural imaging of cardiac electrophysiology on the heart after myocardial infarction. In figure 4.8, we present the heart with infarcted regions. The areas with blue color are indicated as infarcted areas, and the ares with red color are indicated as normal areas. In the heart cycle simulation, the cells within the infarcted areas cannot be excited. Specifically, the parameter a in equation 3.4 was

set with a big value. In figure 4.9, we present the ground truth and the estimated TMP with and without considering cardiac motion. From visual perspective, the two estimated TMPs at time 10ms have very similar pattern. However, they are quite different at time 130ms. Again, the patterns do not reflect the true values of the estimated TMP. As the estimated TMP could be in the different range, we, again, use CC as a metric to measure their similarity with the ground truth. In figure 4.10, we present the reconstructed results with different levels of noise in BSPMs. Overall, the CC values between the reconstruction with fixed geometry and dynamic geometry are quite close at time 10ms. That's because the heart has very little deformation in the dynamic heart model. Nevertheless, the estimated TMP with dynamic heart model are consistently accurate than the ones estimated with static heart model. That's because the heart has large deformation at that time. Estimation of the TMP by using static heart geometry introduced large geometrical errors. Compared to the results of the healthy heart, we find another interesting thing in the heart with myocardial infarction: the difference between CC values at time 10ms and 130ms is much smaller than the difference in the healthy heart. That reason could be that the heart has smaller deformation than the healthy heart, and therefore, has less geometrical error.

4.5 Discussion and conclusion

We investigate the effect of cardiac motion on the forward and inverse problems of cardiac electrophysiology. Through the forward problem, we find the APD of

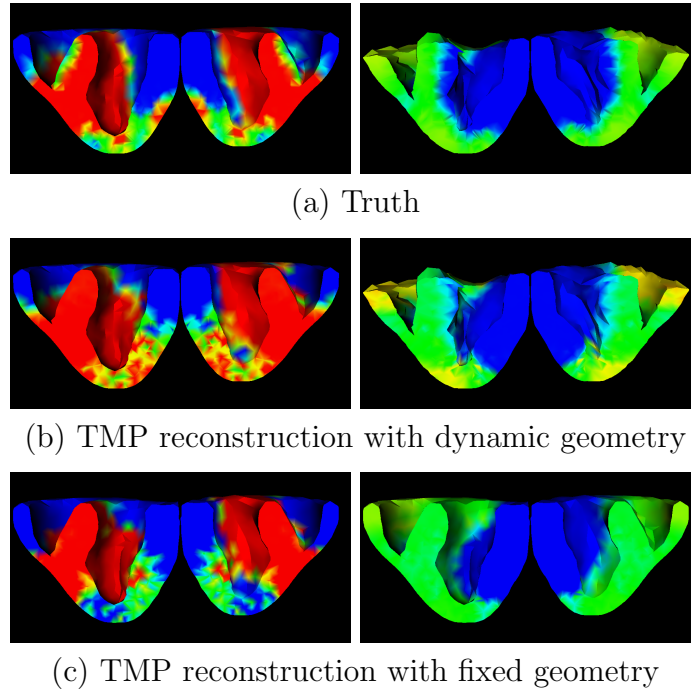


Figure 4.9: TMP reconstruction at different time. Left: 10ms after the onsite of ventricular depolarization; Right: 130ms after the onsite of ventricular depolarization. The colors are manually tuned to have a good visual comparison, they only reflect the pattern of the TMP distribution but not the true value

our electromechanical model is slightly shorter than the simulation by using a heart model with fixed heart geometry. Through the comparison of the simulations of the normal 12-lead ECG, we observed the amplitude of T-wave is increased by using electromechanical model. The cause of these phenomena is the heart has the maximum contraction at the T-wave, and thus the geometrical difference between our model and a static model is maximized at that point.

We also studies the effect of cardiac motion on the inverse problem. We found the estimated results are very similar at depolarization phase when the heart has limited deformation. However, we obtained more accuracy estimation results by

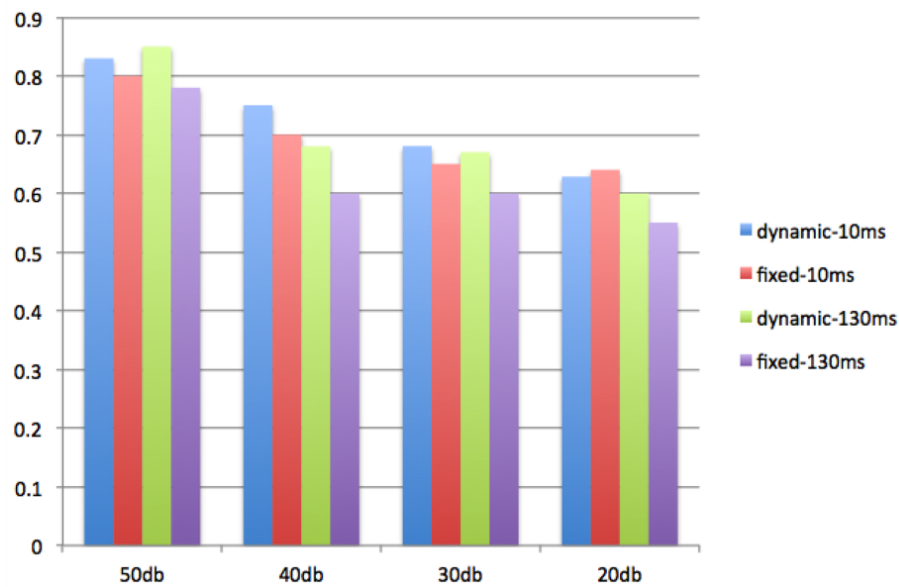


Figure 4.10: Statistical analysis of noninvasive transmural imaging accuracy on the heart with myocardium infarction based on correlation coefficient

considering cardiac motion into account at the repolarization phase. That's because the heart has large deformation at repolarization phase and a big effect of the geometrical error was introduced when the cardiac motion was ignored. As a result, it is important to integrate cardiac electrical and mechanical activities for doing noninvasive transmural imaging of cardiac electrophysiology.

Chapter 5

Understanding of embryonic heart morphogenesis based on robust image segmentation

5.1 Introduction

The heart is the first functioning organ in the embryo. Although the morphology of the heart changes dramatically during development where it transforms from a single tube into a four-chambered pump, the heart functions without interruption to serve as the metabolic needs of the rapidly growing embryo [59]. Embryonic heart morphogenesis (EHM) is critically important for long-time survival, and any defects in the developmental mechanism during embryogenesis may result in congenital cardiac anomalies. In fact, congenital heart disease is relatively frequent which

affects from 19 to 75 per 1000 births in the worldwide, and has been an important cause of childhood morbidity and mortality [60]. Understanding EHM in normal and mal-formed hearts, therefore, has been of considerably clinical and biological interest.

Despite a large body of research in the last decades [61, 62, 63, 64, 65, 66], EHM is still poorly understood mainly because of the complexity of the growing geometry and extremely small size of the developing heart. Thanks to the rapid development of imaging techniques, 3D reconstruction of embryonic hearts from biomedical images has dramatically improved our ability to visualize EHM. Several imaging modalities have been proposed for the study of EHM, however, each of them has its own limitations. Histological sectioning was one of the most widely used approaches for rendering 3D structure of the developing heart [64]. Nevertheless, it needed sophisticated manual alignment of all the sections which was difficult and labor-intensive, and therefore left it only for lab researchers. Optical scanning techniques were also used for rendering 3D/4D volumes of embryonic hearts [67, 65], but low penetration depth limits their application in imaging late stages of embryonic heart development [66]. There were also other imaging modalities used for understanding EHM which, unfortunately, provided very limited spatial resolution[68]. Recently, micro-CT technique was used to image the chambers of embryonic hearts [66]. However, the sophisticated polymerization process ignored the structure of the peripheral luminal space which is actually very important for EHM understanding. Last but not least, all the aforementioned works adopted manual segmentation for 3D heart segmentation due to the lack of appropriate automatic segmentation approaches.

Nevertheless, manual segmentation is tedious, subjective and time-consuming considering the complexity of the developing heart and high resolution images. Thus, an automatic image segmentation method is badly needed.

In view of the problems, we propose a new imaging approach for studying EHM, utilizing tissue optical immersion clearing and 3D confocal microscopy imaging, which can produce high spatial resolution images and achieve large penetration depth at the same time. Furthermore, considering the intensity fall-off in depth nature of confocal microscopy images, we propose a convex active contour model with image depth information for automatic image segmentation. A recently proposed Split-Bregman method was used to minimize the objective function of the model [69, 36]. Embryonic quail hearts at different stages of development were scanned and segmented. Initial heart growth pattern was found through comparison of the structure of hearts at different stages of development. We also quantified the volume change of the whole heart and luminal space from day 6 to day 14 of incubation to provide an insight view of embryonic heart development. Furthermore, realistic continuous growth modeling of the living organs from data sparsely distributed in time has been an emerging field in biomedical field [70, 71], with potential applications to the analysis and prediction of evolving pathologic structures. Thus, this work can be also considered as the first step for data-driven heart growth modeling.

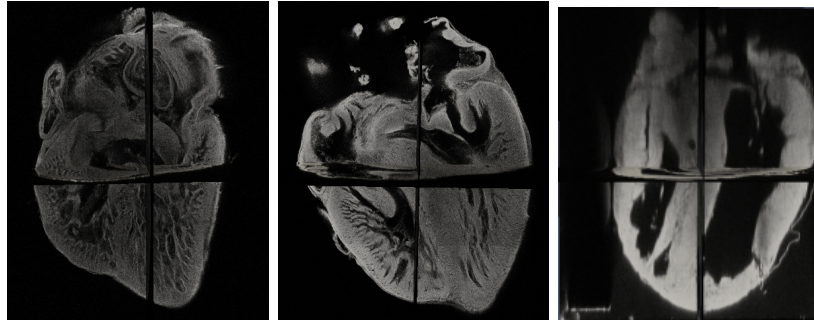


Figure 5.1: 3D view of embryonic quail hearts. From left to right: day 6, day 8 and day 14

5.2 Methodology

The human heart becomes a four-chambered organ by approximately week 8, which is almost the same time the embryo can be visualized through ultrasound, a point that is too late to visualize EHM [72]. We chose quail embryos as our model to study EHM because of their rapid development and short embryonic gestation period (a hatch time of 16.5 days incubation). Except for the time scale, the development of the quail heart parallels that of the human heart.

5.2.1 Image acquisition

Optical imaging method has been widely used as a tool for clinical functional imaging owing to its unique informative features, simplicity, safety and low cost compared to conventional X-ray, MRI and ultrasound imaging. However, the main limitations of optical imaging techniques, including confocal microscopy, are low contrast and spatial resolution, as well as a small probing depth due to strong light scattering in tissue layers [73]. To utilize its strengths and overcome its weaknesses, we combined

confocal microscopy imaging with tissue optical immersion clearing. Optical clearing technique has been used in many areas [73]. However, to the best of our knowledge, this is the first time to use optical clearing with confocal microscopy imaging for EHM study.

In this paper, all the experiments conformed to the *Guide for the Care and Use of Laboratory Animals* (NIH publication No. 85-23, revised 1996). Embryonic hearts were obtained after incubation of Coturnix Japonica (GQF Manufacturing Co., Savannah, GA) or japanese quail eggs to different stages of development. The hearts were stained with di-4-ANBDQBS which was voltage sensitive fluorescent dyes, and then were dehydrated by a graded ethanol series. After dehydration, the hearts were cleared using a 1:2 benzyl alcohol to benzyl benzoate mixture. The cleared heart, which appeared virtually transparent, was stored in the clearing solution until imaging. For image acquisition, the cleared hearts were mounted in a special cuvette and scanned by a Zeiss LSM 510 confocal microscope, with its numerical aperture equals to 0.5 and the radius of back-projected pinhole equals to $2.53nm$. The dye was excited at wave length of $543nm$ and fluorescence recorded the wave length above $560nm$ using a long-pass filter. For more details of heart preparation and imaging, we refer the readers to [74].

High spatial resolution images were obtained after heart scanning, which had an intra-slice pixel size of $1.75\mu m \times 1.75\mu m$ and inter-slice pixel size $12.9000\mu m$. In Fig.5.1, we present 3D view of three hearts at day 6, 8, and 14 respectively. From the images, the evolution of the luminal space of the heart from spongy structure to well-separated chamber structure can be clearly observed.

5.2.2 Image formation

In a confocal microscope, a pinhole is used to reject most out-of focus light. Thus, the amount of light reaching the detector is low, and the noise statistics can be well described by a Poisson process [75]. A general image formation model can be represented as the following equation

$$I_0(x) = n([h * I](x)) \quad (5.1)$$

where $x \in \Omega$ is a point in the image domain. I_0 is an observed image. I is an ideal image. h is a point spread function (PSH). $*$ means convolution operation. n models the noise distribution. Based on our imaging setting, the PSF of the microscope is very small compared to our voxel size, and therefore the effect of convolution by PSF can be ignored. In the work, we used median filter to smooth the observed image, and assume the noise in the smoothed image can be considered as additive zero mean Gaussian distribution. Thus the final image formation can be represented as the following equation

$$\tilde{I}_0 \approx I + \mathbf{n} \quad (5.2)$$

where \tilde{I}_0 and \mathbf{n} represent smoothed image and image noise respectively.

5.2.3 Image Segmentation

The purpose of image segmentation is to find a partition $\psi(\Omega)$ of the image domain Ω and recover the ideal image I as well. Under the assumption that the intensity distribution of the ideal image is piecewise constant, Chan-Vese (CV) model with level set implementation was proposed and has been widely used for image segmentation [76]. Later on, this model was further extended to global CV (G-CV) model by transforming it into a global convex optimization problem [77]. However, confocal microscopy images is characterized by intensity fall-off in depth, which makes G-CV model unsuitable for this purpose. To solve this problem, we further assume the ideal image can be described as the multiplication of an intensity piecewise constant image c and a depth-related bias field b

$$I = \sum_{i=1}^N (c_i \cdot u_i) \cdot b_i \quad (5.3)$$

where N is number of regions in the image, and u_i is an image partition function. Under this assumption, we developed a new convex active contour model for automatic segmentation of confocal microscopy images. The model can be represented as the following equation

$$\begin{aligned} \min_{u \in [0,1]} E(c_1, c_2, u) &= \int_{\Omega} |\nabla u(x)| + \lambda \int_{\Omega} (\tilde{I}_0(x) - I_1(x))^2 u(x) dx \\ &+ \lambda \int_{\Omega} (\tilde{I}_0(x) - I_2(x))^2 (1 - u(x)) dx \end{aligned} \quad (5.4)$$

The first term on the right side of equation (5.4) is a L1 total variation (TV) norm which is used for smoothing the variable u . The second and third terms are data fidelity terms which keep the intensity distribution of the ideal images close to the original image. Here, u is a partition variable, and λ is a weighting constant to keep the balance among the three terms on the right side of equation (5.4). $I_1(x) = c_1 \cdot \gamma^{z(x)}$ and $I_2(x) = c_2 \cdot \gamma^{z(x)}$ are two ideal images represent the intensity on two different subregions. $\gamma^{z(x)}$ is a depth-dependent bias field to characterize the intensity fall-off in depth property of the images, where z is the position of the point x in z-direction and γ is an experimentally determined decreasing constant.

There are total three unknown variables in our model: c_1 , c_2 , and u . By using first variation with respect to c_1 and c_2 , we can obtain

$$c_1 = \frac{\int_{x \in \Omega} u(x) \tilde{I}_0(x) \gamma^{z(x)} dx}{\int_{x \in \Omega} u(x) \gamma^{2z(x)} dx} \quad (5.5)$$

$$c_2 = \frac{\int_{x \in \Omega} (1 - u(x)) \tilde{I}_0(x) \gamma^{z(x)} dx}{\int_{x \in \Omega} (1 - u(x)) \gamma^{2z(x)} dx} \quad (5.6)$$

To minimize the equation (5.4) with respect to u , we adopt the fast and efficient Split Bregman method proposed in [69, 36]. Split Bregman method does not require regularization, continuation or the enforcement of inequality constraints, and it is very efficient for solving L1-regularized optimization problems like equation (5.4). For easier description of Split Bregman method, we rewrite the form of equation

(5.4)

$$\min_{u \in [0,1]} E = \int_{\Omega} |\nabla u(x)| + \lambda e_r(x)u(x) dx \quad (5.7)$$

where $e_r(x) = (\tilde{I}_0(x) - I_1(x))^2 - (\tilde{I}_0(x) - I_2(x))^2$.

Here, the term $\lambda \int_{\Omega} (\tilde{I}_0(x) - I_2(x))^2 dx$ has been ignored because it does not include the variable u .

To minimize equation (5.7) with respect to u , we introduce an auxiliary variable d , such that $d = \nabla u$. Thus, the problem of minimization the energy function of equation (5.7) becomes to minimize the following energy function

$$\min_{u \in [0,1], d} \int_{\Omega} |d| + \lambda e_r(x)u(x) dx, \text{ with } d = \nabla u \quad (5.8)$$

To solve the constrained problem in equation (5.8), we use Split Bregman method. The problem becomes to solve the following sequence of optimization problems

$$(u^{k+1}, d^{k+1}) = \arg \min_{u \in [0,1], d} \int_{\Omega} |d| + \lambda e_r(x)u(x) + \frac{\mu}{2} |d - \nabla u - b^k|^2 dx \quad (5.9)$$

$$b^{k+1} = b^k + \nabla u^{k+1} - d^{k+1} \quad (5.10)$$

Here, $k = 0, 1, 2, \dots$, the third term on the right side of equation (5.9) is used to enforcing the constraint $d = \nabla u$. b^k is the Bregman vector. μ and λ are two constant

weighting parameters to keep a balance of two terms. To solve equation (5.9), we adopt the alternating minimization scheme. First, we consider the minimization of equation (5.9) with respect to u . The minimizing solution u^{k+1} is characterized by the optimality condition:

$$\lambda \nabla u = \lambda e_r + \mu \operatorname{div}(b^k - d^k), u \in [0, 1] \quad (5.11)$$

By using Gauss-Seidel iterative scheme, we can get an approximate solution for a 3D variable u^{k+1} . ($i = 0, 1, 2, \dots$)

$$\begin{aligned} \zeta_{l,m,n} &= d_{l-1,m,n}^{x,k} - d_{l,m,n}^{x,k} - b_{l-1,m,n}^{x,k} + b_{l,m,n}^{x,k} + d_{l-1,m,n}^{y,k} - d_{l,m,n}^{y,k} - b_{l-1,m,n}^{y,k} + b_{l,m,n}^{y,k} \\ &+ d_{l-1,m,n}^{z,k} - d_{l,m,n}^{z,k} - b_{l-1,m,n}^{z,k} + b_{l,m,n}^{z,k} \end{aligned} \quad (5.12)$$

$$\begin{aligned} \phi_{l,m,n} &= \frac{1}{6}(u_{l-1,m,n}^{k+1,i} + u_{l+1,m,n}^{k+1,i} + u_{l,m-1,n}^{k+1,i} + u_{l,m+1,n}^{k+1,i} + u_{l,m,n-1}^{k+1,i} \\ &+ u_{l,m,n+1}^{k+1,i} + \zeta_{l,m,n} - \frac{\lambda}{\mu} e_{r(l,m,n)}) \end{aligned} \quad (5.13)$$

$$u_{l,m,n}^{k+1,i+1} = \max\{\min\{\phi_{l,m,n}, 1\}, 0\} \quad (5.14)$$

where i is the iteration index for Gauss-Seidel iterative method, l, m, n are the indices of the voxel in axis x, y , and z respectively. $u_{l,m,n}^{k+1,0} = u_{l,m,n}^k$.

After calculating an approximate u^{k+1} , we can obtain d^{k+1} by minimizing the equation (5.9) with respect to d

$$d^{k+1} = \frac{\nabla u^{k+1} + b^k}{|\nabla u^{k+1} + b^k|} \max(|\nabla u^{k+1} + b^k| - \frac{1}{\lambda}, 0) \quad (5.15)$$

Once u^{k+1} and d^{k+1} are available, the Bregman vector b^k can be updated according to the equation (5.10). For more details of 2D Split Bregman method, we refer the readers to [69].

As a summary, the procedures of using Split Bregman method to solve equation (5.8) contains the following steps:

- (1) Initialization: initial b^0 , d^0 and u^0 .
- (2) Fix u , calculate c_1 and c_2 according to equation (5) and (6), and further calculate e_r .
- (3) Update u^{k+1} by solving equations (5.12), (5.13), and (5.14).
- (4) Update d^{k+1} by solving equation (5.15).
- (5) Update b^{k+1} by solving equation (5.10).
- (6) Convergence test: test whether a stable solution u has reached. if not, go to step (2).
- (7) The objects are detected by thresholding $\Sigma = \{x : u(x) > \alpha\}$, where $\alpha \in [0, 1]$. In this paper, we choose $\alpha = 0.5$.

Table 5.1: DSC values that measure the overlap between the two manual segmentation, the first manual segmentation against automatic segmentation, and the second manual segmentation against automatic segmentation

	day 6	day 7	day 8	day 9	day 14
biologist 1 vs biologist 2	0.75	0.79	0.85	0.87	0.93
automatic vs biologist 1	0.65	0.72	0.78	0.85	0.88
automatic vs biologist 2	0.68	0.75	0.79	0.81	0.91

5.3 Experimental results

5.3.1 Data

In this study, we selected three groups of quail hearts. Each group had five embryonic quail hearts at the development stage of day 6, 7, 8, 9 and 14 respectively. All the hearts were processed and imaged according to section 2.1. The image size varied from 768 x 768 x 112 (day 6) to 3075 x 2560 x 478 (day 14). To build a database of manual segmentation for reference, we invited two biologists to independently segment the hearts manually with the software ITK-SNAP [78]. Due to the large size of the image and the complexity of the heart geometry, it typically took a biologist more than one week to finish one heart segmentation. For this reason, we currently only selected one group for manual segmentation.

5.3.2 Evaluation of automatic segmentation

Fig.5.2 shows one 3D and three 2D slice views of the quail heart at day 14 with two manual segmentations and one automatic segmentation. Although the image

exhibits severe intensity inhomogeneity, visual inspection of the results shows that automatic segmentation can correctly capture most of the structures of the heart as manual segmentation. The most difference between manual and automatic segmentation occurs at the regions above the atrioventricular valve which can be observed in both 3D and 2D views. That's mainly because the contrast is very low at this region, automatic segmentation algorithm only uses image information can not detect the boundary precisely, while biologists using their knowledge can manually locate the boundary. What's more, we have also observed the presence of small objects within the heart chambers only detected by automatic segmentation. These small objects could be papillary muscle that can be considered as either a part of the myocardium or a part of the blood pool. As a result, both manual and automatic segmentation for these small objects are acceptable.

We also quantitatively evaluate our algorithm by measuring the the overlap of automatic segmentation and manual segmentation by using Dice's similarity coefficient (DSC). For two segmentations S_1 and S_2 , the DSC value is defined as $2|S_1 \cap S_2|/(|S_1| + |S_2|)$. The DSC value is normalized, where 0 indicates complete dissimilarity and 1 indicates complete agreement. The overlap values reflecting the variability between the manual segmentation by two biologists are listed in the second row of Table 5.1. Except for day 6 and 7, all the DSC values are greater than 0.85, which means there is sufficient level of reliability for the two manual segmentations. The reason of low DSC values at day 6 and 7 is that the geometry of the hearts at these days are very complex as shown in Fig.5.3, and thus it is difficult for the biologists to achieve high agreement. The overlap comparison between auto-

matic and manual segmentation are listed in the third and fourth row of Table 5.1. Similarly, we can find the DSC values are low at day 6 and 7 and high at the rest. Overall, the overlap measures show that the automatic segmentation method has similar level of variability to the manual segmentation, which means our automatic segmentation method is applicable for EHM study.

5.3.3 EHM study

Fig.5.3 shows automatic segmentation results of one group of hearts. As we can see, an obvious phenomenon of early heart development is the morphology evolution of the ventricles. The left and right ventricles are merged together and exhibit sponge network structure at day 6 and 7 as the result of cardiac looping [62]. The interventricular septum starts to grow between day 7 and day 8, as the ventricles are partially separated at day 8. At day 9, the interventricular septum eventually forms and divide the ventricles into the left and right ventricle. However, the two ventricles still present some sponge structure at day 9. The shape of the ventricles eventually become mature at day 14.

We also quantify the average volume of the whole heart and the luminal space at different stages of development based on the segmentation results. We use the open source VTK library (www.vtk.org) to calculate the average volume, and list the average volume values in Table5.2. We find that the average volume of the whole heart and the luminal space increased from 2.6 mm^3 to 77.5 mm^3 and 0.41 mm^3 to 20.2 mm^3 respectively, which is nearly two order of magnitude increase in an incubation period of approximate 10 days. This finding is the similar in range

Table 5.2: Average volume of the whole heart and the luminal space at different stages of development. (mm^3)

	day 6	day 7	day 8	day 9	day 14
Total heart	2.6	3.4	6.0	10.2	77.5
Luminal space	0.41	0.62	0.75	1.74	20.2

as the findings in [66]. Furthermore, we also find the average volume of the whole heart grows faster than the luminal space, which means that the myocardium grows towards both inside and outside.

5.4 Conclusion

We proposed an imaging approach and a novel automatic segmentation method for EHM study. We demonstrated the applicability of our imaging method to capture the 3D structure of embryonic quail hearts, and also proved the efficiency of our segmentation algorithm for EHM study in both visual inspection and quantitative analysis. Based on the findings from EHM study, we believe this work could help us to further understand the fundamental mechanisms of embryonic heart development.

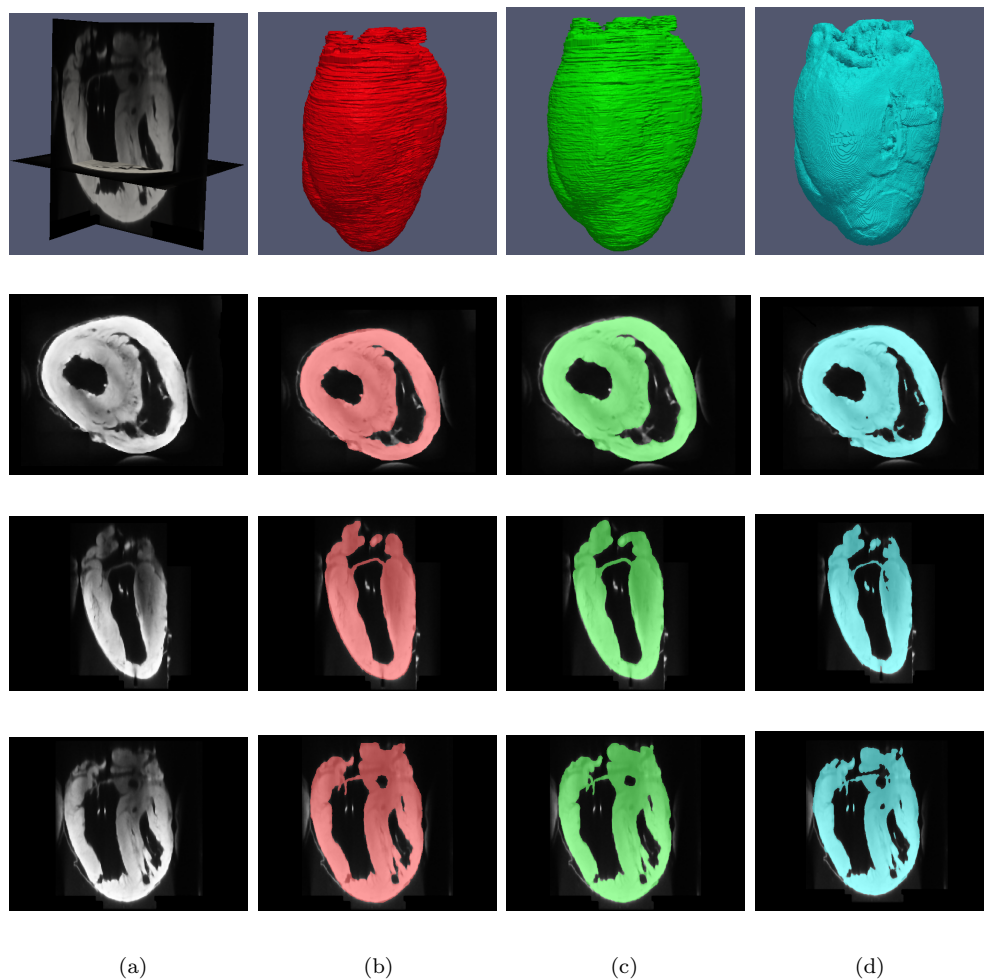


Figure 5.2: Visual comparison between manual segmentation and automatic segmentation. (a) original 3D image and three slices in different views. (b) manual segmentation done by the first biologist. (c) manual segmentation done by the second biologist. (d) automatic segmentation.

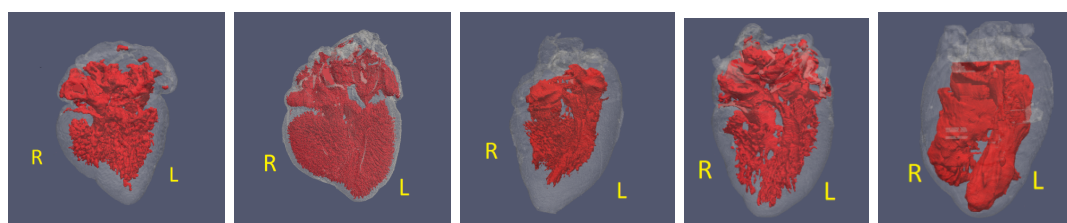


Figure 5.3: 3D segmentation of one group of the hearts. Columns from left to right are the heart at day 6, 7, 8, 9 and 14. For visualization purpose, the outer boundary is rendered as transparent. (L: left ventricle. R: right ventricle)

Chapter 6

Summary and future work

The contributions of this thesis are in threefold: first, we developed a biologically-inspired mathematical model for simulation of cardiac electromechanics. The model can be used to simulate the heart under physiological and pathological conditions that can be used as a testing environment in research and clinical studies. Second, we investigated the effect of cardiac motion on noninvasive transmural imaging of cardiac electrophysiology, and found that cardiac motion did have an effect to the noninvasive estimation of cardiac electrophysiology when the heart has large deformation. Thus, it is important to use a electromechanically integrated way to estimate cardiac electrophysiology from BSPMs. Besides understanding the interconnection relationship between electrical and mechanical functions, we also investigate the longitudinal morphogenesis of embryonic heart, which could pave the road for growth heart modeling in our future work.

6.1 Modeling of cardiac electromechanics

Cardiac electromechanical model is critical for understanding the mechanisms behind heart activities and consistently improve heart diagnosis techniques. The proposed model has been validated as a useful platform for simulation of the heart activities under physiological and pathological conditions. We believe this model will be very useful to help us understand the mechanisms behind various heart behaviors, such as cardiac desynchronization. Because we have adopted phenomenological models for both electrical and mechanical components, its physiological meaningfulness and computational feasibility could pave the road for simultaneous reconstruction of cardiac electromechanics from multi-modality clinical measurements.

Although the model is very promising, there are still some perspectives need to be improved in the future. First, our model is a generic model, the parameters of the model are adopted from literature [42, 22], thus it can only be used to simulate some general conditions. The simulation results are not personalized. In fact, model personalization has been a hot topic in cardiac research recently [20, 19, 79]. To overcome this shortcoming, one possible solution is to estimate personalized parameters from clinical measurements by solving inverse problems [20, 19].

Second, each component of our proposed model may not be the best ones for mathematically describing the heart behaviors. For example, the cardiac electrophysiology component used in our model can not simulate realistic ST segment in the ECG signals. What's more, some nonlinear material properties are said to be better for describing the heart behavior [11].

Third, we have simplified the effect of mechanoelectrical feedback by only con-

sidering the effect of heart deformation on the position of electrical source. The realistic mechanoelectrical feedback simulation can be achieved through including stretch-activated channels (SACs) into the model[31, 38]. However, this type of models usually contain a lot of parameters and are much more complex than phenomenological models. For clinical usage, computational heart models need to have fewer parameters and low computational cost.

Fourth, computational cost is always an issue for cardiac research on modeling and simulation. In current work, we have adopted PETSc for CPU parallel programming [81]. A possible way to speed up the simulation is to implement the algorithms on GPU, which has been adopted by some groups for cardiac modeling [82].

6.2 The effect of cardiac motion on noninvasive transmural imaging of cardiac electrophysiology

The experimental results demonstrated that the effect of cardiac motion on noninvasive transmural imaging of cardiac electrophysiology is limited during depolarization phase, because the heart has limited deformation at that time. However, it does have an effect during the repolarization phase, because the heart has large deformation in this period. Our current conclusions are based on synthetic experiments, further validation on real data will be our future work. What's more, this step could pave the road to building an electromechanically integrated framework for simultaneous

cardiac electrical and mechanical activities estimation.

6.3 Understanding of embryonic heart morphogenesis from segmentation of microscopy confocal images

Besides cardiac electromechanics, we also investigated longitudinal cardiac anatomy in embryonic heart. By combining confocal microscopy imaging with optical clearing, our method was able to achieve penetration depth over $6mm$ that enabled us to acquire volumetric images of the developing heart through the whole incubation period. We believe this imaging data can help biologists to understand more details of early heart development and investigate events that lead to congenital heart defects.

Image segmentation is always a headache for researchers in this field because of the complexity of the developing geometry. The convex active contour model proposed in this paper was a first step towards automatic segmentation in EHM study, and showed promising results. One significant challenge in developing heart segmentation is the lack of a gold standard. Due to the expensive labor cost to label the images, we provided limited validation in the paper. In the future, we will build a larger manually segmented database for segmentation algorithm validation. What's more, this database could also be used for training and testing parameter-free machine learning algorithms.

The ultimate goal of this work will be heart growth modeling. Due to the complexity of developing heart, current heart growth modeling mainly focus on very early stages of EHM [83]. To the best of our knowledge, there does not exist any works on modeling the whole EHM process from the single tube shape to four-chambered shape. With EHM knowledge from EHM study, we will work towards data-driven heart growth modeling.

Bibliography

- [1] J. Constantino, Y. Hu, and N. Trayanova, “A computational approach to understanding the cardiac electromechanical activation sequence in the normal and failing heart, with translation to the clinical practice of crt,” *Progress in Biophysics and Molecular Biology*, vol. 110, pp. 372–379, 1012.
- [2] Z. Zheng, J. Croft, W. Giles, and G. Mensah, “Sudden cardiac death in the united states,” *Circulation*, vol. 104, pp. 2158–2163, 2001.
- [3] D. Noble, “A modification of the hodgkin-huxley equations applicable to purkinje fibre action and pacemaker potentials,” *The journal of physiology*, vol. 160, pp. 317–352, 1962.
- [4] D. Durrur, R. Dam, G. Freud, M. Janse, F. Meijler, and R. Arzbaecher, “Total excitation of the isolated human heart,” *Computational Methods in Applied Mechanics and Engineering*, vol. 41, pp. 899–912, 1970.
- [5] F. Badke, P. Boinay, and J. Covell, “Effects of ventricular pacing on regional left ventricular performance in the dog,” *American Journal of Physiology: Heart and Circulatory Physiology*, vol. 238, pp. 858–867, 1980.

- [6] M. Guccione and A. McCulloch, “Mechanics of active contraction in cardiac muscle: constitutive relations for fibre stress that describe deactivation,” *Journal of Biomechanical Engineering*, vol. 115, pp. 72–81, 1993.
- [7] B. He, G. Li, and X. Zhang, “Noninvasive imaging of cardiac transmembrane potentials within three-dimensional myocardium by means of a realistic geometry anisotropic heart model,” *IEEE Transaction on Biomedical Engineering*, vol. 50, no. 10, pp. 1190–1202, 2003.
- [8] N. Smith, A. McCulloch, and D. Paterson, “What can modelling provide to cardiac physiology,” *The Journal of Physiology*, vol. 590, pp. 4401–4402, 2012.
- [9] E. Shapiro, “The first textbook of electrocardiography, thomas lewis: Clinical electrocardiography,” *Journal of the American college of cardiology*, vol. 1, no. 4, pp. 1160–1161, 1983.
- [10] S. Dixit and D. Callans, “Mapping for ventricular tachycardia,” *Cardiac electrophysiology review*, vol. 6, pp. 436–441, 2002.
- [11] K. Wong, L. Wang, H. Zhang, and P. Shi, “Physiological fusion of functional and structural data for cardiac deformation recovery,” *Medical Image Computing and Computer Assisted Intervention*, vol. 25, pp. 159–166, 2010.
- [12] J. Kim, N. Kang, H. Lee, and J. Kim, “Computational modeling and analysis for left ventricle motion using ct/echo image fusion,” *SPIE Proceeding*, vol. 9036, 2014.

- [13] M. Carbayo, J. Kybic, A. Santos, M. Suhling, P. Hunziker, and M. Unser, “Spatio-temporal nonrigid registration for ultrasound cardiac motion estimation,” *IEEE Transactions on Medical Imaging*, vol. 24, no. 9, pp. 1113–1126, 2005.
- [14] M. Lab, P. Taggart, and F. Sachs, “Mechano-electric feedback,” *Cardiovascular Research*, vol. 33, pp. 1–2, 1996.
- [15] P. Kohl and U. Ravens, “Cardiac mechano-electric feedback: past, present and prospect,” *Progress in Biophysics and Molecular Biology*, vol. 82, pp. 3–9, 2003.
- [16] E. T. et al., *Textbook of cardiovascular medicine: second edition*. Wiley, 2000.
- [17] R. Schimpf, C. Antzelevitch, D. Haghi, C. Giustetto, A. Pizzuti, F. Gaita, C. Veltmann, C. Wolpert, and M. Borggrefe, “Electromechanical coupling in patients with the short qt syndrome: Further insights into the mechano-electrical hypothesis of the u wave,” *Heart Rhythm*, vol. 5, pp. 241–245, 2008.
- [18] K. Wong, L. Wang, H. Zhang, H. Liu, and P. Shi, “Physiological fusion of functional and structural data for cardiac deformation recovery,” *IEEE Transactions on Medical Imaging*, vol. 30, pp. 990–1000, 2011.
- [19] K. Wong, “From medical images to individualized cardiac mechanics: A physiome approach,” *Thesis*, 2010.
- [20] ———, “Personalized noninvasive imaging of volumetric cardiac electrophysiology,” *Thesis*, 2009.

- [21] H. Mao, L. Wang, C. Wang, H. Liu, and P. Shi, “A coupled heart-torso framework for cardiac electrocardiographic simulation,” *Computing in Cardiology*, vol. 38, pp. 225–228, 2011.
- [22] M. Sermesant, H. Delingette, and N. Ayache, “An electromechanical model of the heart for image analysis and simulation,” *IEEE Transactions on Medical Imaging*, vol. 25, pp. 612 – 625, 2006.
- [23] P. Pathmanathan and J. Whiteley, “A numerical method for cardiac mechanoelectric simulations,” *Functional Imaging and Modeling of the Heart*, pp. 357–365, 2009.
- [24] D. Wang, R. Kirby, R. Macleod, and C. Johnson, “Inverse electrocardiographic source localization of ischemia: An optimization framework and finite element solution,” *Journal of Computational Physics*, vol. 250, pp. 403–424, 2013.
- [25] R. Kerckhoffs, S. Healy, T. Usyk, and A. Mcculloch, “Computational methods for cardiac electromechanics,” *Proceedings of IEEE*, vol. 94, pp. 769–783, 2006.
- [26] L. Wang, H. Zhang, K. Wong, H. Liu, and P. Shi, “Physiological-model-constrained noninvasive reconstruction of volumetric myocardial transmembrane potentials,” *IEEE Transaction on Biomedical Engineering*, vol. 57, pp. 296–315, 2010.
- [27] O. Camara, M. Sermesant, P. Lamata, L. Wang, M. Pop, J. Relan, M. D. Craene, H. Delingette, H. Liu, S. Niederer, G. P. A. Pashaei and, D. Romero, R. Sebastian, K. Wong, H. Zhang, N. Ayache, A. Frangi, P. Shi, N. Smith, and

- G. Wright, “Inter-model consistency and complementarity: Learning from ex-vivo imaging and electrophysiological data towards an integrated understanding of cardiac physiology,” *Progress in Biophysics and Molecular Biology*, 2011, 122-133.
- [28] D. Chapelle, M. Fernandez, J. Gerbeau, P. Moireau, J. Marie, and N. Zenzemi, “Numerical simulation of the electromechanical activity of the heart,” *Functional Imaging and Modeling of the Heart*, vol. 5528, pp. 357–365, 2009.
- [29] M. Nash and A. Panfilov, “Electromechanical model of excitable tissue to study reentrant cardiac arrhythmias,” *Progress in Biophysics and Molecular Biology*, vol. 85, pp. 501–522, 2004.
- [30] S. Goktepe and E. Kuhl, “Electromechanics of the heart: a unified approach to the strongly coupled excitation-contraction problem,” *Computational Mechanics*, vol. 45, pp. 227–243, 2010.
- [31] N. Traynova, J. Constantino, and V. Gurev, “Models of stretch-activated ventricular arrhythmias,” *Journal of Electrocardiology*, vol. 43, pp. 479–485, 2010.
- [32] D. Keller, O. Jarrousse, T. Fritz, and S. Ley, “Impact of physiological ventricular deformation on the morphology of the t-wave: a hybrid, static-dynamic approach,” *IEEE Transaction on Biomedical Engineering*, vol. 58, pp. 2109–2119, 2011.

- [33] M. Jiang, G. Shou, Q. Wei, F. Liu, and S. Crozier, “Effect of cardiac motion on solution of the electrocardiography inverse problem,” *IEEE Transaction on Biomedical Engineering*, vol. 56, pp. 923–931, 2009.
- [34] R. Throne and L. Olson, “The effects of errors in assumed conductivities and geometry on numerical solutions to the inverse problem of electrocardiography,” *IEEE Transaction on Biomedical Engineering*, vol. 42, no. 12, pp. 1192–1200, 1995.
- [35] F. Sachse, *Computational Cardiology: Modeling of Anatomy, Electrophysiology, and Mechanics*. Springer, Heidelberg, 2004.
- [36] H. Mao, H. Liu, and P. Shi, “A convex neighbor-constrained active contour model for image segmentation,” *IEEE International Conference on Image Processing*, pp. 793–796, 2010.
- [37] M. Cerqueira, N. Weissman, V. Dilsizian, A. Jacobs, S. Kaul, W. Laskey, D. Pennell, J. Rumbergen, T. Ryan, and M. Verani, “Standardized myocardial segmentation and nomenclature for tomographic imaging of the heart: a statement for healthcare professionals from the cardiac imaging committee of the council on clinical cardiology of the american heart association,” *Circulation*, vol. 105, pp. 539–542, 2002.
- [38] Y. Rudy, M. Ackerman, D. Bers, C. Clancy, S. Houser, B. London, A. McCulloch, D. Przywara, R. Rasmusson, R. Solaro, N. Trayanova, D. Wagoner, A. Varro, J. Weiss, and D. Lathrop, “Systems approach to understanding elec-

- tromechanical activity in the human heart: a national heart, lung, and blood institute workshop summary,” *Circulation*, vol. 118, pp. 1202–1211, 2008.
- [39] A. Hodgkin and A. Huxley, “A quantitative description of membrane current and its application to excitation and conduction in nerve,” *The Journal of Physiology*, vol. 117, pp. 500–544, 1952.
- [40] R. FitzHugh, “Impulses and physiological states in theoretical models of nerve membranes,” *Biophysical journal*, vol. 1, pp. 445–466, 1961.
- [41] C. Luo and Y. Rudy, “A model of the ventricular cardiac action potential. depolarization, repolarization, and their changes,” *Circulation Research*, vol. 68, pp. 1501–1526, 1991.
- [42] R. Aliev and A. Panfilov, “A simple two-variable model of cardiac excitation,” *Chaos, Solitons Fractals*, vol. 7, no. 3, pp. 293–301, 1996.
- [43] J. Rogers and A. McCulloch, “A collocation-galerkin finite element model of cardiac action potential propagation,” *IEEE Transaction on Biomedical Engineering*, vol. 41, no. 8, pp. 743 – 757, 1994.
- [44] C. Mitchell and D. Schaeffer, “A two-current model for the dynamics of cardiac membrane,” *Bulletin of Mathematical Biology*, vol. 65, pp. 767–793, 2003.
- [45] F. Sachse, G. Seemann, K. Chaisaowong, and D. Weiss, “Quantitative reconstruction of cardiac electromechanics in human myocardium: Assembly of electrophysiologic and tension generation models,” *The Journal of Cardiovascular Electrophysiology*, pp. 210–218, 2003.

- [46] J. Keener, *Mathematical physiology of the heart*. Springer, New York, 1998.
- [47] M. Gurev, M. Maleckar, and N. Trayanova, “Cardiac defibrillation and the role of mechanoelectric feedback in postshock arrhythmogenesis,” *Annals of the New York Academy of Sciences*, vol. 1180, pp. 320–333, 2006.
- [48] K. C. Wong, “From medical images to individualized cardiac mechanics: A physiome approach,” *Ph.D dissertation, Rochester Institute of Technology*, 2010.
- [49] K. Bathe, *Finite Element Procedures*. Prentice Hall, Englewood Cliffs, 1996.
- [50] G. Liu, *Mesh free methods*. CRC Press, 2002.
- [51] M. Nash, “Mechanics and material properties of the heart using an anatomically accurate mathematical model,” *Ph.D dissertation, University of Auckland*, 1998.
- [52] J. Dolbow and T. Belytschko, “An introduction to programming the meshless element free galerkin method,” *Archives of Computational Methods in Engineering*, vol. 5, no. 3, pp. 207–241, 1998.
- [53] , “<http://www.healthanalytics.us/2013/11/04/the-heart-a-sacred-object-or-a-marvel-of-bioengineering/>,” *healthanalytics*, 2014.
- [54] J. Xu, A. Rahimi, F. Gao, and L. Wang, “Noninvasive transmural electrophysiological imaging based on minimization of total-variational functional,” *IEEE Transactions on Medical Imaging*, 2014.

- [55] A. Rahimi, J. Xu, and L. Wang, “Lp-norm regularization in volumetric imaging of cardiac current sources,” *Computational and mathematical methods in medicine*, 2013.
- [56] L. Wang, H. Zhang, K. Wong, and P. Shi, “Coupled meshfree-bem platform for electrocardiographic simulation: Modeling and validations,” *Medical Imaging and Augmented Reality*, vol. 5128, pp. 98–107, 2008.
- [57] “Physionet/computers in cardiology challenge 2007: electrocardiographic imaging of myocardial infarction,” <http://www.physionet.org/challenge/2007>.
- [58] N. Smith, M. Buist, and A. Pullan, “Altered t wave dynamics in a contracting cardiac model,” *The Journal of Cardiovascular Electrophysiology*, vol. 14, pp. 203–209, 2003.
- [59] J. Icardo and F. Manasek, “Cardiogenesis: development mechanisms and embryology,” *The heart and cardiovascular system*, pp. 1563–1586, 1992.
- [60] W. H. Organization, “Global atlas on cardiovascular disease prevention and control,” *Expert Review of Medical Devices*, pp. 1–164, 2011.
- [61] J. Lacktis and F. Manasek, “An analysis of deformation during a normal morphogenic event,” *Morphogenesis and Malformation of the Cardiovascular System*, vol. 17, pp. 205–227, 1978.
- [62] L. Taber, B. Keller, and E. Clark, “Cardiac mechanics in the stage-16 chick embryo,” *Journal of Biomechanical Engineering*, vol. 114, pp. 427–434, 1992.

- [63] M. Liebling, J. Vermot, and S. Fraser, “Double time-scale image reconstruction of the beating and developing embryonic zebrafish heart,” *IEEE International Symposium on Biomedical Imaging*, pp. 855–858, 2008.
- [64] B. Groenendijk, B. Hierck, J. Vrolijk, M. Baiker, M. Pourquie, A. Gittenberger, and R. Poelmann, “Changes in shear stress-related gene expression after experimentally altered venous return in the chicken embryo,” *Circulation Research*, vol. 96, pp. 1291–1298, 2005.
- [65] M. Liebling, A. Forouhar, R. Wolleschensky, B. Zimmermann, R. Ankerhold, S. Fraser, M. Gharib, and M. Dickinson, “Rapid three-dimensional imaging and analysis of the beating embryonic heart reveals functional changes during development,” *Developmental Dynamics*, vol. 235, pp. 2940–2948, 2006.
- [66] J. Butcher, D. Sedmera, R. Guldborg, and R. Markwald, “Quantitative volumetric analysis of cardiac morphogenesis assessed through micro-computed tomography,” *Developmental Dynamics*, vol. 236, pp. 802–809, 2007.
- [67] M. Jenkins, F. Rothenberg, D. Roy, V. Nikolski, Z. Hu, M. Watanabe, D. Wilson, I. Efimov, and A. Rollins, “4d embryonic cardiography using gated optical coherence tomography,” *Optics Express*, vol. 14, pp. 736–748, 2006.
- [68] B. Smith, “Magnetic resonance microscopy in cardiac development,” *Microscopy Research and Technique*, vol. 52, pp. 323–330, 2001.
- [69] T. Goldstein and S. Osher, “The Split Bregman method for L1 regularized problems,” *SIAM Journal on Imaging Sciences*, vol. 2, pp. 323–343, 2009.

- [70] J. Fishbaugh, M. Prastawa, S. Durrleman, J. Piven, and G. Gerig, “Analysis of longitudinal shape variability via subject specific growth modeling,” *Medical Image Computing and Computer Assisted Intervention*, pp. 731–738, 2012.
- [71] S. Durrleman, X. Pennec, A. Troune, G. Gerig, and N. Ayache, “Spatiotemporal atlas estimation for developmental delay detection in longitudinal datasets,” *Medical Image Computing and Computer Assisted Intervention*, pp. 297–304, 2009.
- [72] K. Fong, A. Toi, S. Salem, L. Hornberger, D. Chitayat, S. Keating, F. Mcauliffe, and J. Johnson, “Detection of fetal structural abnormalities with us during early pregnancy,” *Radiographics*, vol. 24, pp. 157–174, 2004.
- [73] E. Genina, A. Bashkatov, and V. Tuchin, “Tissue optical immersion clearing,” *Expert Review of Medical Devices*, vol. 7, no. 6, pp. 825–842, 2010.
- [74] S. Niederer and N. Smith, “An improved numerical method for strong coupling of excitation and contraction models in the heart,” *Progress in Biophysics and Molecular Biology*, vol. 96, pp. 90–111, 2008.
- [75] N. Dey, L. Feraud, C. Zimmer, P. Roux, Z. Kam, J. Marin, and J. Zerubia, “Richardsonlucy algorithm with total variation regularization for 3d confocal microscope deconvolution,” *MICROSCOPY RESEARCH AND TECHNIQUE*, vol. 69, pp. 260–266, 2006.
- [76] T. Chan and A. Vese, “Active contours without edges,” *IEEE Transactions on Image Processing*, vol. 10, pp. 266–276, 2001.

- [77] X. Bresson, S. Esedoglu, P. Vandergheynst, J. Thiran, and S. Osher, “Fast global minimization of the active contour/snake model,” *Journal of Mathematical Imaging and Vision*, vol. 28, pp. 151–167, 2007.
- [78] P. A. Yushkevich, J. Piven, H. Cody Hazlett, R. Gimpel Smith, S. Ho, J. C. Gee, and G. Gerig, “User-guided 3D active contour segmentation of anatomical structures: Significantly improved efficiency and reliability,” *Neuroimage*, vol. 31, no. 3, pp. 1116–1128, 2006.
- [79] M. Sermesant, R. Chabiniok, P. Chinchapatnam, T. Mansi, F. Billet, P. Moireau, J. P. K. Wong, J. Relan, K. Rhode, M. Ginks, P. Lambiase, H. Delingette, M. Scoringe, C. Rinaldi, D. Chapelle, R. Razavi, and N. Ayaiche, “Patient-specific electromechanical models of the heart for the prediction of pacing acute effects in crt: a preliminary clinical validation,” *Medical Image Analysis*, pp. 201–215, 2011.
- [80] P. Chinchapatnam, K. Rhode, M. Ginks, C. Rinaldi, P. Lambiase, R. Razavi, S. Arridge, and M. Sermesant, “Model-based imaging of cardiac apparent conductivity and local conduction velocity for diagnosis and planning of therapy,” *IEEE Transactions on Medical Imaging*, vol. 27, pp. 1631–1642, 2008.
- [81] S. Balay, S. Abhyankar, M. F. Adams, J. Brown, P. Brune, K. Buschelman, V. Eijkhout, W. D. Gropp, D. Kaushik, M. G. Knepley, L. C. McInnes, K. Rupp, B. F. Smith, and H. Zhang, “PETSc users manual,” no. ANL-95/11 - Revision 3.5, 2014. [Online]. Available: <http://www.mcs.anl.gov/petsc>

- [82] G. Viguera, I. Roy, A. Cookson, J. Lee, N. Smith, and D. Nordsletten, “Toward gpgpu accelerated human electromechanical cardiac simulations,” *Numerical Methods and Applications of Multi-Physics in Biomechanical Modeling*, vol. 30, pp. 4117–134, 2012.
- [83] S. Goenezen, M. Rennie, and S. Rugonyi, “Biomechanics of early cardiac development,” *Biomechanics and Modeling in Mechanobiology*, vol. 11, pp. 1187–1204, 2012.